

**THÈSE DE DOCTORAT
DE SORBONNE UNIVERSITÉ**

Spécialité : Physique

École doctorale n°564: Physique en Île-de-France

réalisée

au Laboratoire Kastler Brossel

sous la direction de Pierre-François Cohadon

présentée par

Pierre-Edouard Jacquet

pour obtenir le grade de :

DOCTEUR DE SORBONNE UNIVERSITÉ

Sujet de la thèse :

Squeezed light optomechanics: Theory and Experiments

soutenue le 26 Février 2026

devant le jury composé de :

M ^{me}	Agnès MAITRE	PU	INSP (SU)	Présidente
M	Pierre VERLOT	MC	LuMIn (UPSaclay)	Rapporteur
M	Jean-Pierre ZENDRI	DR	INFN (UPadova)	Rapporteur
M ^{me}	Sara DUCCI	PU	MPQ (UPCité)	Examinaterice
M	Jack HARRIS	PU	Yale University	Examinateur
M	Pierre-François COHADON	MC	LKB (ENS)	Directeur



Remerciements

Merci bien

Contents

I Experiments: Optomechanics	3
I.1 System Description and Setup	4
I.1.1 Previous LKB work and Motivation	4
I.1.2 Specifications and Design	5
I.1.3 Flexure Actuation	9
I.1.4 Experimental Setup	11
I.1.5 Alignment Procedures	13
I.2 Experimental Characterization	14
I.2.1 Cavity Scans	14
I.2.2 Cavity Locking and Mechanical Characterization	23
I.2.3 Bistability	27
I.2.4 Discussion & Perspectives	27
I.3 Optomechanical Fibered Cavity	30
I.3.1 Design considerations	31
I.3.2 Fiber mirror fabrication	35
I.3.3 Designs and optical layout	37
I.4 Conclusion	41
Appendix A: Two-photon derivations	43

Field Quantization	43
Two photon formalism	45
Derivation of the optimal angle	51
Appendix B: Error Signals	53
Direct detection error signals	53
PDH error signal	55
Appendix C: Three Mirror cavities	59
Bibliography	65

Chapter I

Experiments: Optomechanics

This chapter will cover the experimental methods used in the development of optomechanical three-mirror cavity systems, focusing on the design, fabrication, and characterization of mechanical resonators within optical cavities. The methods are designed to enhance the sensitivity of measurements in quantum optics and optomechanics.

Contents

I.1	System Description and Setup	4
I.1.1	Previous LKB work and Motivation	4
I.1.2	Specifications and Design	5
I.1.3	Flexure Actuation	9
I.1.4	Experimental Setup	11
I.1.5	Alignment Procedures	13
I.2	Experimental Characterization	14
I.2.1	Cavity Scans	14
I.2.2	Cavity Locking and Mechanical Characterization	23
I.2.3	Bistability	27
I.2.4	Discussion & Perspectives	27
I.3	Optomechanical Fibered Cavity	30
I.3.1	Design considerations	31
I.3.2	Fiber mirror fabrication	35
I.3.3	Designs and optical layout	37
I.4	Conclusion	41

Over the past two decades, optomechanical systems have greatly benefited from advancements in optical coating technologies, enabling the realization of high-finesse cavities ($\mathcal{F} > 10^6$) [1, 2]. Simultaneously, progresses in micro/nanofabrication allowed the making of mechanical structures with high Q factors ($> 10^8$) [3, 4]. Despite these achievements, a significant challenge remained: fabricating mechanical elements that possess both high Q and high reflectivity, as optical, mechanical and thermal effects often degrade system performance and hinder ultra-sensitive measurements.

I.1 System Description and Setup

I.1.1 Previous LKB work and Motivation

Previous optomechanics experiments at LKB have primarily utilized Fabry–Pérot cavities with two mirrors, where the end mirror of the cavity was typically a HR mirror deposited on top of a mechanical structure featuring a mechanical mode of interest.

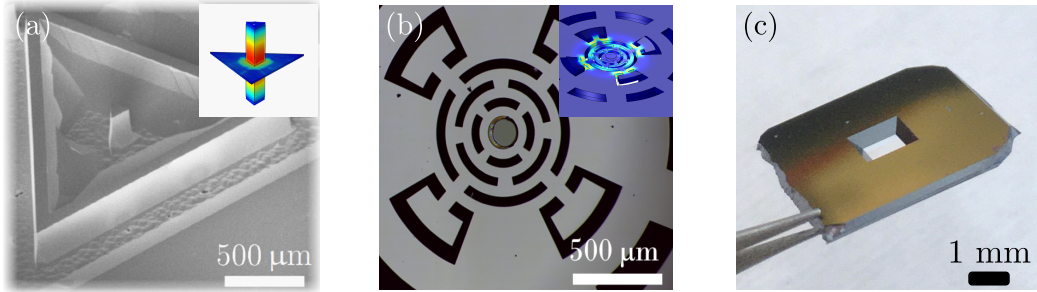


Fig. I.1 Mechanical resonators developed at LKB over the years for optomechanics experiments. (a) Quartz micropillar resonator studied over A. Kuhn L. Neuhaus PhD work. (b) Suspended silicon disk resonator studied over R. Metzdorff and M. Croquette PhD works. (c) Silicon Nitride membrane resonator developed in-house and used in this work.

Over A. Kuhn and L. Neuhaus PhD works, the group, in collaboration with ONERA developed a platform based on a 1-mm-thick quartz micropillar with an effective mass of $33 \mu\text{g}$. The structure supports a fundamental compression mode oscillating at 3.6 MHz, with a mode shape shown in Fig. I.1.(a). Using a dry-film photoresist technique, a $100 \mu\text{m}$ diameter high-reflectivity mirror was deposited on one end of the pillar. Careful design of the suspension has yielded mechanical quality factors up to 3×10^6 at room temperature and up to 7×10^7 below 1 K. When integrated into a $50 \mu\text{m}$ -long Fabry–Pérot cavity with a custom-fabricated coupling mirror, finesse exceeding 10^5 were achieved. Importantly, this compact cavity remains robust against vibrations of the dilution refrigerator and maintains

alignment during cooldown, thereby providing a stable platform to study optomechanical effects in the intermediate mass regime. [limitations and why it didnt work](#)

Then over R. Metzdorff and M. Croquette PhDs, another resonator was developed in collaboration with Francesco Marin's team, based on a suspended silicon disk shown in Fig. I.1.(b). The device operates in a balanced mode, where the central disk vibrates in opposition to four surrounding counterweights. By adjusting the geometry, the resonance frequency was increased to 280 kHz, corresponding to an effective mass of about $110 \mu\text{g}$, bringing the system closer to the micropillar parameters. A HR mirror was then deposited on top using the same technique as the micropillar. Finesse of about ~ 50000 were then reached. At cryogenic temperature, optimized designs reached mechanical quality factors on the order of 1.2×10^6 .[limitations and why it didnt work](#)

Although the systems ended up being limited by various factors mentioned above (optical, mechanical and thermal effects), the parts designed over the years did feature a high level of passive stability as well as good thermalization properties. A pivotal step was demonstrated by Harris and co-workers [5, 6], who decoupled optical and mechanical requirements by placing a high- Q membrane resonator within a rigid, high-finesse cavity, using the intracavity field to probe and control the resonator's dynamics. Such a resonator, a SiN membrane, is shown in Fig. I.1.(c).

I.1.2 Specifications and Design

It was then decided to build on this design and extend it to a three-mirror cavity in a MATE configuration to benefit from this large linear and tunable coupling range as detailed in the previous chapter. That is the work Michael and myself undertook during my M2 internship and the following years of my PhD. This new three mirror cavity then needed to fulfill various requirements detailed in what follows.

High Finesse

Low loss mirrors were produced by **Jérôme DEGALLAIX** and **David HOFMAN** at the *Laboratoire des Matériaux Avancés* (LMA, Lyon) using ion-beam-sputtered (IBS) Bragg stacks made of Ta_2O_5 (high index, $n \approx 2.09$) and SiO_2 (low index, $n \approx 1.46$) [7, 8]. The coatings were deposited in the LMA's Veeco *SPECTOR* chambers and subsequently annealed at 500°C for 10 hours to minimise both optical (absorption) and mechanical losses, following the recipe of Amato *et al.*.

We supplied the LMA with a batch of substrates with various radii of curvature to explore

different cavity geometries. The requested specifications are summarized in the table below. The total round-trip scatter and absorption losses are usually below 20 ppm, in agreement with the measurements reported (absorption ~ 0.7 ppm, scattering ~ 10 ppm).

Substrate type	Laseroptik ID	R	Front-side HR T	Back-side AR
Plane	S-00798	∞ (plane)	20 ± 45 ppm	$R \lesssim 100$ ppm
Plano-concave	S-00128	-25 mm	$100, 50 \pm 10$ ppm	$R \lesssim 100$ ppm
Plano-concave	S-00127	-15 mm	$100, 50 \pm 10$ ppm	$R \lesssim 100$ ppm
Plano-concave	S-00126	-10 mm	$100, 50 \pm 10$ ppm	$R \lesssim 100$ ppm

Table I.1: Specifications of supplied Laseroptik substrates for different cavity geometries.

The quarter-wave design is centred at $\lambda = 1064$ nm for normal incidence. After annealing, the measured mechanical loss angle of the $\text{TiO}_2:\text{Ta}_2\text{O}_5/\text{SiO}_2$ stack is $\phi < 4 \times 10^{-4}$ at 1 kHz [link to mechanical damping needed](#), supporting cavity finesse in the range $200\,000 - 500\,000$ before excess scatter or absorption dominates [[AmatoPhD](#)].

High Q factor

Two different square membranes were used in the MATE cavities, both made of high-stress silicon nitride (Si_3N_4), a material known for its excellent mechanical properties, including high tensile stress and low intrinsic mechanical loss, making it ideal for optomechanical applications [[SiN_review](#)], and of nominal side lengths $l_n \times l_m = 500 \mu\text{m} \times 500 \mu\text{m}$.

The first membrane was made in-house at LKB by **Thibaut Jacqmin** and **Himanshu Patange** during Himanshu's PhD work. The silicon wafer was $350 \mu\text{m}$ thick, and the SiN layers thicknesses was nominally 100 nm. Starting with the silicon wafer/chip coated with SiN on both sides, a photoresist is patterned by lithography to define a square window. Reactive-ion etching (RIE) then opens a square window through the top SiN layer. The exposed silicon is then wet-etched in KOH from the opened side until the cavity breaks through, leaving a released, free-standing SiN membrane spanning the opening. The membrane is then cleaned using HF to remove any residuals from the fabrication process. This very process etches the SiN layer as well, resulting in a final membrane thickness of less than 100nm. For detailed fabrication steps, refer to Himanshu's PhD thesis [9]. We nonetheless succinctly display the fabrication steps in Fig I.2.

The second membrane is a commercially Norcada[®] (NX10050AS) [10] SiN square membrane, specifically marketed as a *high Q* standard membrane for optomechanics applications. It features a Silicon frame of $200 \mu\text{m}$ thickness, and a SiN layer of nominal thickness 50 nm. Regarding the quality factor, literature reports:

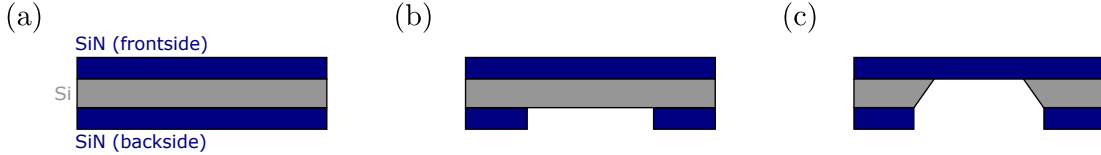


Fig. I.2 *Fabrication steps of the SiN membrane resonator used in the MATE cavity.* (a) starting from a silicon wafer coated with SiN on both sides. (b) lithography and RIE to open a square window in the top SiN layer. (c) KOH wet etching from the opened side until the cavity breaks through, leaving a free-standing SiN membrane. The membrane is then cleaned using HF to remove any residuals from the fabrication process.

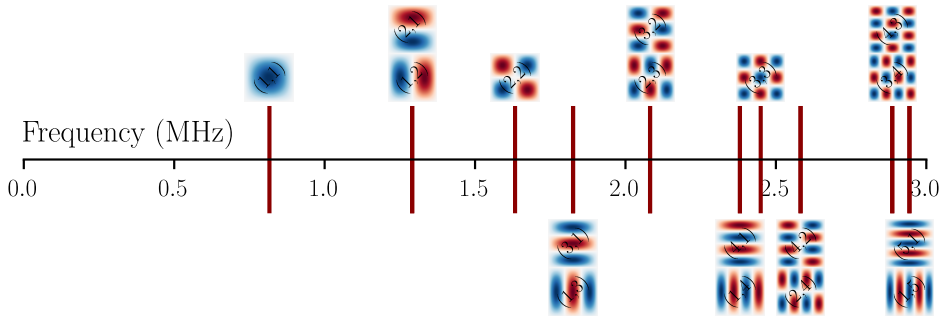


Fig. I.3 *Simulated mode shapes and frequencies of a square SiN membrane of side length $500\mu\text{m}$ under high tensile stress ($\sigma \sim 1 \text{ GPa}$).*

- **Room temperature.** Measurements on similar Norcada membranes report quality factors $Q \sim 5 \times 10^6$ at $\approx 1 \text{ MHz}$ in $< 10^{-6} \text{ mbar}$ vacuum [11, 5].
- **Cryogenic operation.** Cooling to $T \lesssim 300 \text{ mK}$ reduces internal friction by an order of magnitude, with $Q > 10^7$ routinely observed [SiN_cryogenic].

The membrane's high stress, thin-film nature and dielectric composition make it fully compatible with ultra-high-vacuum environments and repeated cryogenic cycling, while introducing (a priori) negligible optical loss in the cavity. The expected mechanical mode structure can be derived from

$$f_{n,m} = \sqrt{\frac{\sigma}{4\rho} \left(\left(\frac{n}{l_n}\right)^2 + \left(\frac{m}{l_m}\right)^2 \right)} \quad (\text{I.1})$$

with $\rho \sim 3 \text{ g/cm}^3$ the film mass density, $\sigma \sim 1 \text{ GPa}$, (n, m) the mode indices, and (l_n, l_m) the membrane side lengths. Considering a square membrane of identical side lengths of $500\mu\text{m}$ yields a fundamental mode frequency at $f_{1,1} \sim 816 \text{ kHz}$, with the two higher order modes $(1, 2)$ and $(2, 1)$ degenerate at $f_{1,2} \sim f_{2,1} \sim 1.29 \text{ MHz}$ etc.. We display the first few mode shapes and expected frequencies in Fig. I.3.

Optical alignment

The cavity is designed to be compatible with the Thorlabs® cage system. The input mirror is mounted on a 3 axis cage mount, allowing for easy alignment of the input mirror with respect to the cavity optical axis. Both the resonator and the back mirror are embedded within a custom-made holder, which is itself integrated into the cage system. The relative tilt between the resonator and the back mirror is adjusted using a set of 3 screws with a very fine thread, allowing for a fine alignment of the parallelism of the back cavity. The alignment procedure is detailed in section I.1.5.

Dynamical range

The input mirror is glued to a PI Ceramic® P-016.00H ring-stack piezoelectric actuator using vacuum epoxy (Torr Seal®). Driven from 0 to +1000 V it provides a longitudinal stroke of $5\ \mu\text{m}$, a blocking force of $2.9\ \text{kN}$, as well as an unloaded resonance of $144\ \text{kHz}$, making it suitable for fast, low-noise cavity-length control.

The end-mirror–membrane assembly is mounted on a custom holder actuated by three PD080.31 piezo chips arranged mechanically in series. Each chip yields $2\ \mu\text{m}$ of travel over a drive range of -20 to $+100\ \text{V}$; the triple stack therefore supplies roughly $6\ \mu\text{m}$ of coarse tuning while preserving high stiffness and sub-microsecond response. The effective range is lower than this owing to the fact the piezo is constrained within the holder. Furthermore, one should not constrain the piezo to much to avoid damaging it: it happened that the assembly was too tightly screwed in such that it ended up fracturing the piezo pushing against the back mirror holder. An easy workaround would be to add some elastic spacer between the piezo and the copper piece (like kapton tape for example).

Combining the $5\ \mu\text{m}$ stroke of the front P-016.00H with the $6\ \mu\text{m}$ range of the rear triple stack provides an overall cavity-length adjustment sufficient to scan few FSRs, as well as to tune the membrane position over a full wavelength, thus accessing allowing exploration of the three mirror cavity physics.

Compactness & Stability

The entire assembly is built as a cage system using standard Thorlabs® cage parts, allowing for a compact and stable assembly. The cage system also allows for (relatively) easy alignment of the mirrors, as well as easy access to the piezo actuators.

Vacuum and Cryogenic compatibility

The back cavity composed of the back mirror and the middle mirror is embedded inside an Oxygen Free Copper (OFC) assembly with a circular geometry, eventually mitigating for transverse misalignment issues when going to cryogenic temperatures, the constraints compensating themselves radially with respect to the symmetry axis of the cavity assembly[[OFHC_review](#)]. Furthermore, the screws used to hold the assembly together are made of brass with a thermal expansion coefficient lower than that of the OFC, tightening up the cavity when reaching cryogenic temperatures. Thorlabs cage parts are compatible with moderate vacuum operation down to $\sim 10^{-7}$ mbar if properly degreased and ultrasound cleant, but a custom cryocompatible system to hold the input mirror would be needed for operation at cryogenic temperatures.

The initial design of the cavity was made using Autodesk Fusion 360, allowing for a detailed 3D model of the entire assembly, including the piezo actuators, the mirrors and the cage system. The design was then exported to a STEP file format, which was used to manufacture the parts using a 3 axis CNC milling machine and a digital lathe. The pieces were machined by **Carounagarane DORE** and **Gael COUPIN** at the LKB mechanical workshop with $100\mu\text{m}$ tolerance. A detailed view of the cavity design and assembly is shown in Fig. I.4.

I.1.3 Flexure Actuation

One specificity of the MATE system is that the back cavity is significantly shorter than the front cavity, which would require high precision in both the machining of the copper pieces and the positioning of the resonator. In our case, we aim at a centimetric cavity which would require to position the membrane at roughly hundreds of microns from the back mirror, and parallel to the back mirror. Moving the membrane independently from the back mirror while maintaining a controllable tilt between both planes is therefore challenging.

A smart workaround was introduced by Jack Sankey and its group [[12](#)], where the authors introduced a flexure-tuned MATE system. The key innovation lies in actuating the membrane position by flexing its supporting silicon frame rather than translating the entire mount. This is done by mounting the back cavity in a semi-monolithic fashion, and 'locking' the silicon frame of the membrane using three screws with a fine thread, allowing for a fine adjustment of the angle of the membrane plane with respect to the back mirror plane. The piezos pushing on the back of the assembly then force the silicon frame constrained by the screws to bend, thus displacing the membrane with respect to the back mirror, as shown in Fig. I.5. This approach preserves the cavity alignment for gentle flexures, while enabling

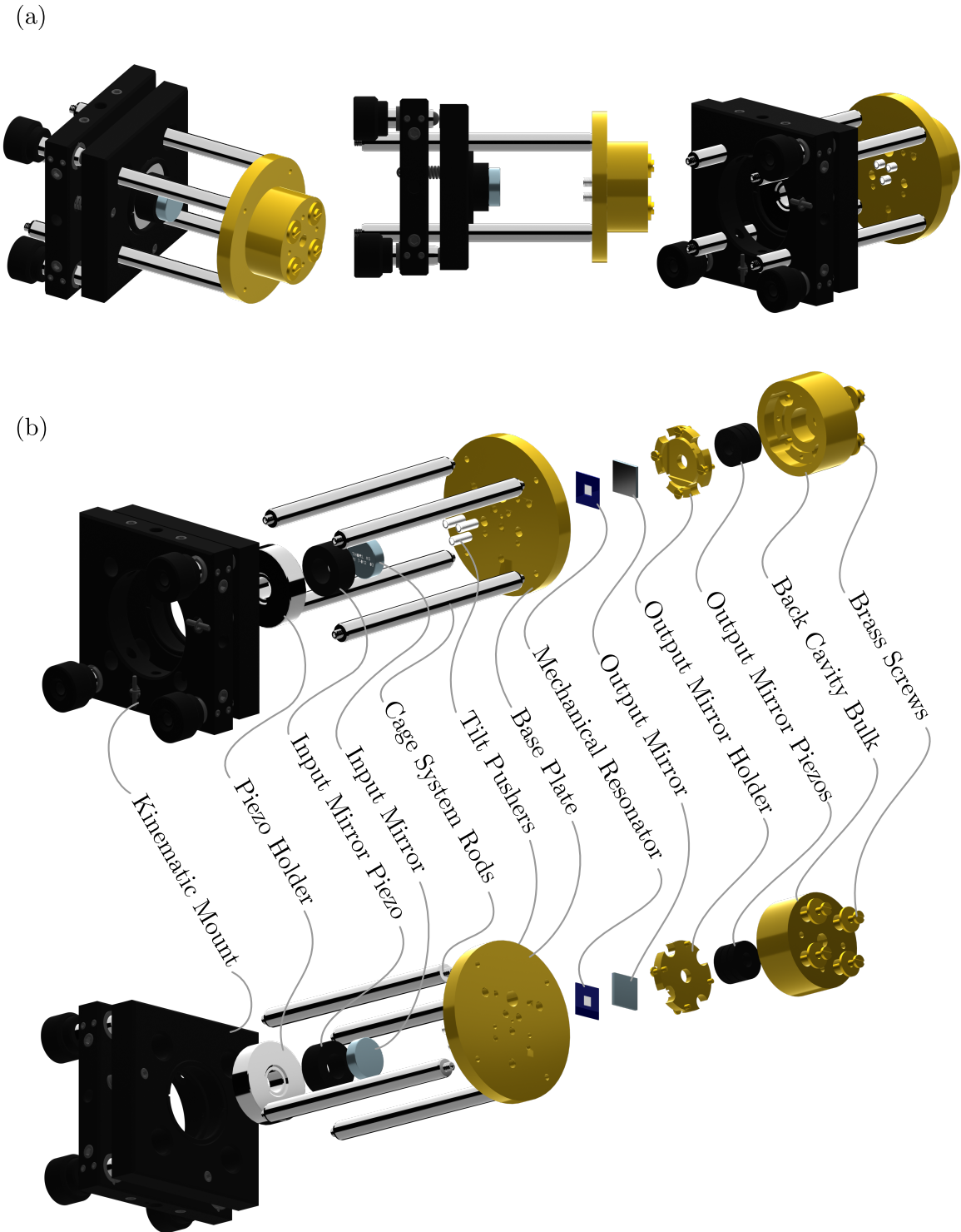


Fig. I.4 Cavity design and assembly. (a) The figure shows the overall assembly of the MATE system from various views, highlighting the integration of the high-finesse mirrors, the membrane resonator embedded inside the back cavity copper assembly held to the input mirror Thorlabs holder through a cage system.(b) The exploded view details the arrangement of the mechanical and optical components, illustrating the modular design that facilitates alignment, stability, and compatibility with vacuum environments.

continuous and wide-range tuning of both the membrane displacement and tilt.

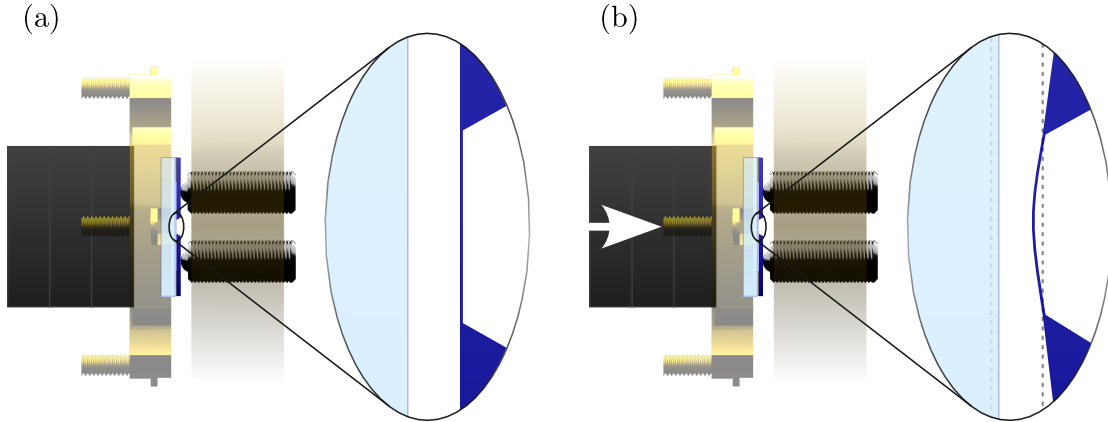


Fig. I.5 Cavity design and assembly. (a) In this configuration (no voltage applied to the piezos), the screws are used to align the membrane plane with respect to the back mirror plane, ensuring a good parallelism between both planes. (b) Flexure tuning of the membrane position. When a voltage is applied to the piezos, they push on the back of the assembly, forcing the silicon frame to bend, thus displacing the membrane with respect to the back mirror. The two dashed lines show the initial positions of the back mirror and the membrane. This push shortens the overall cavity length (i.e. increasing the overall system's frequency), as well as the relative distance between the mirror and the membrane (i.e. changing the optomechanical coupling).

I.1.4 Experimental Setup

The assembly is now to be integrated into the optical setup shown in Fig. I.6, as well as schematically in Fig. I.7. The source laser is a 1064nm Nd:YAG laser (Coherent Mephisto). We did not require the full optical power delivered by the laser, so a short optical path not detailed here splits the laser in 3 arms to eventually fiber couple some laser power and bring it to other experiments that would need 1064nm laser light.

The optical path then consists of :

- a first half waveplate and a beam splitter to adjust the total power injected into the experimental setup,
- a fibered electro-optics phase modulator (EOM Photline NIR-MPX-LN-10) to generate sidebands for the PDH locking of the cavity. It is polarization matched by using a

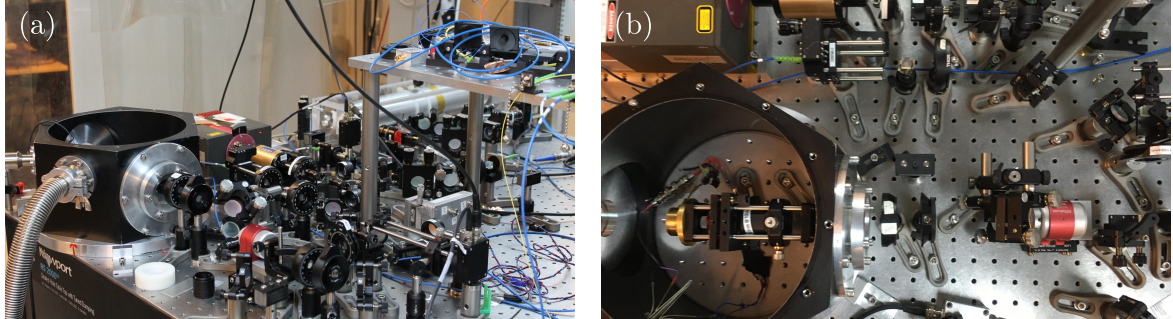


Fig. I.6 *Pictures of the optical setup used for the MATE cavity experiments. (a) Overall view of the optical table, with the laser source in the back, the optical path in the middle, and the vacuum tank on the left. (b) Top view of the MATE cavity mounted inside the vacuum tank, with AR coated windows to allow for optical access.*

fibered polarization controller to avoid Residual Amplitude Modulation noise (RAM) at the output (three blue circles on the optical layout).

- a fiber coupler to go from a guided optical mode to a free space optical mode, with a the coupler adjusted such that the outputted beam is collimated and has a waist of about 1mm,
- a quarter waveplate to compensate for ellipticity of the output beam polarization, then a half waveplate and a beam splitter to adjust the powers injected into the cavity path and the prospective LO path, respectively,
- on the cavity path, a faraday rotator to ensure the cavity reflected beam to be deflected to an output port and not back into the fiber
- a lens to mode match the laser input mode to the cavity mode, with a focal length of 40 to 60mm depending on the input mirror radii of curvature. This lens is mounted on a x-y cage system translation mount, and is mounted inside the vacuum chamber that features AR coated windows to allow for optical access yet minimal parasite reflections.
- the cavity itself.
- two photodiodes (Thorlabs ???) to detect the reflected beam and the transmitted beam, respectively, with 40mm focal length lenses to focus the beam onto the photodiodes.

The optical path was designed to be as modular as possible, allowing for easy replacement of the components if needed, as well as additions of optical elements. For this reason, it features two faint additional optical paths as seen on Fig. I.7, one for a prospective LO, and another to deflect the reflected beam to a Homodyne Detection setup using a flip mirror.

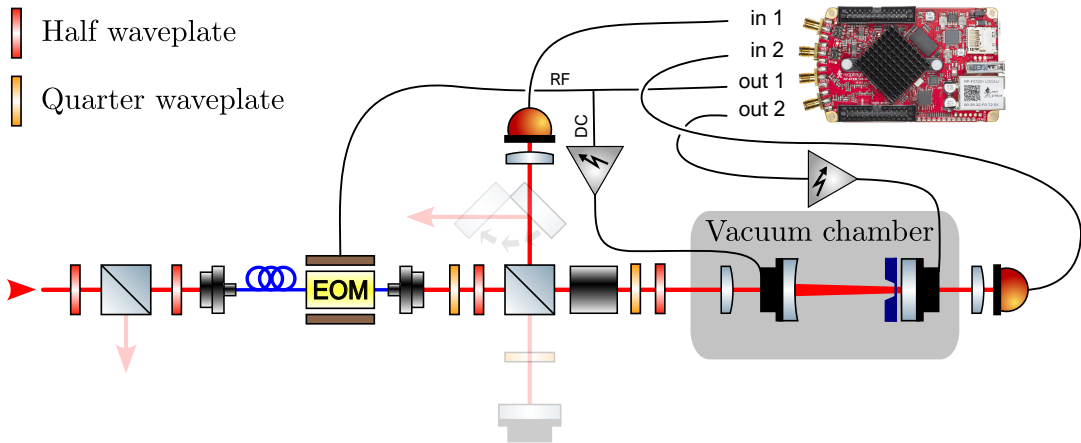


Fig. I.7 Schematic of the optical layout used for the MATE cavity experiments. The various optical components are detailed in the main text. The transparent lines show two additional optical paths that were not used during this thesis, one for a prospective LO, and another to deflect the reflected beam to a Homodyne Detection setup using a flip mirror.

Polarization optics would also need to be added on the Homodyne Detection path to mix the LO and the reflected beam, but this was not done during this thesis.

I.1.5 Alignment Procedures

The optical setup is now to be aligned as to ensure a good mode matching between the laser input mode and the cavity mode. The steps are as follows, and the associated diagrams are shown in Fig. I.8:

- **Step 1** (Fig. I.8(a)): we position an iris diaphragm before our two injection mirrors mounted on (θ_x, θ_y) kinematic mounts. We then adjust the tilt of both mirrors i.e. *beam-walking*, such that the reflected beam is centered on the iris diaphragm: this is done by maximising the reflected signal on the reflection photodiode. This ensures the beam reflected by the output mirror (HR mirror) is at normal incidence. In a second time we tune the plane of the resonator using the three screws of the assembly. We monitor the Fizeau fringes in transmission with a camera (Allied Vision Alvium), and adjust the tilt such that no fringes are to be seen.
- **Step 2** (Fig. I.8(b)): we then place the focusing lens in the optical path, and adjust its position such that we recover maximal power on the reflection photodiode. This lens is mounted on the (x-y) cage system translation mount, and positioned at a distance from the back mirror fixed by the cavity mode matching requirements (ref chap theory). The lens is then fixed in place using the cage system screws.

- **Step 3** (Fig. I.8(c)): we add the input mirror on a (θ_x, θ_y) cage system mount, and adjust its position to get an input beam normal to the tangent of the concave mirror curvature. This is also done maximising the reflected power on the reflection photodiode. The mount (and thus the mirror) was also positioned at the appropriate distance from the back mirror to ensure optimal mode matching.
- **Step 4** (Fig. I.8(d)): We scan the cavity length using the piezo actuator mounted on the input mirror, and monitor the cavity resonances using both the reflected and transmitted photodiodes. We finally fine tune the mode match by *beam-walking* the two injection mirrors. We can also play with the collimating lens at the fiber coupler (not shown on the diagram) as to fine tune for longitudinal mode matching. The cavity is now aligned and ready for operation.

I.2 Experimental Characterization

I.2.1 Cavity Scans

Once the cavity is aligned, we can scan the cavity length by driving the front mirror piezo with a triangular or a sine wave voltage. This signal is first amplified using a high voltage amplifier made by the LKB electronic workshop, which can deliver up to 1000V. The output impedance of the amplifier is a standard 50 Ohms, but the piezo in parallel at the end of the line with capacitance of about 15 nF low pass filters the signal at ~ 200 Hz. We can also modulated the back piezo actuators, in DC or AC, and a similar lowpass filtering occurs with a lower cutoff frequency ~ 50 Hz (3 piezo actuators in parallel with a capacitance of around 100 nF each).

We then monitor the cavity resonances using both the reflected and transmitted photodiodes and scanning the cavity over a large range, as to mode match the cavity to the TEM₀₀ mode. By beam walking, we optimally mode match the cavity such that higher order modes vanish in the photodiode noise floor and the reflected and transmitted signals are maximised, we can then perform finer scans to characterize the cavity parameters. We observed that putting the cavity under vacuum did sometimes misalign the cavity, such that even mode matching to our best ability using two mirrors outside the vacuum tank did not yield a perfect TEM₀₀ match. We also saw some membranes/phononic crystals break throughout the pumping process, most likely due to dust or degazing of the setup.

Once aligned and mode matched, we can proceed to the cavity characterization. Over the course of my PhD, few *functional* cavities were mounted inside the vacuum tank. We chose to only present the results for two of these, as to display various physical effects observed. The

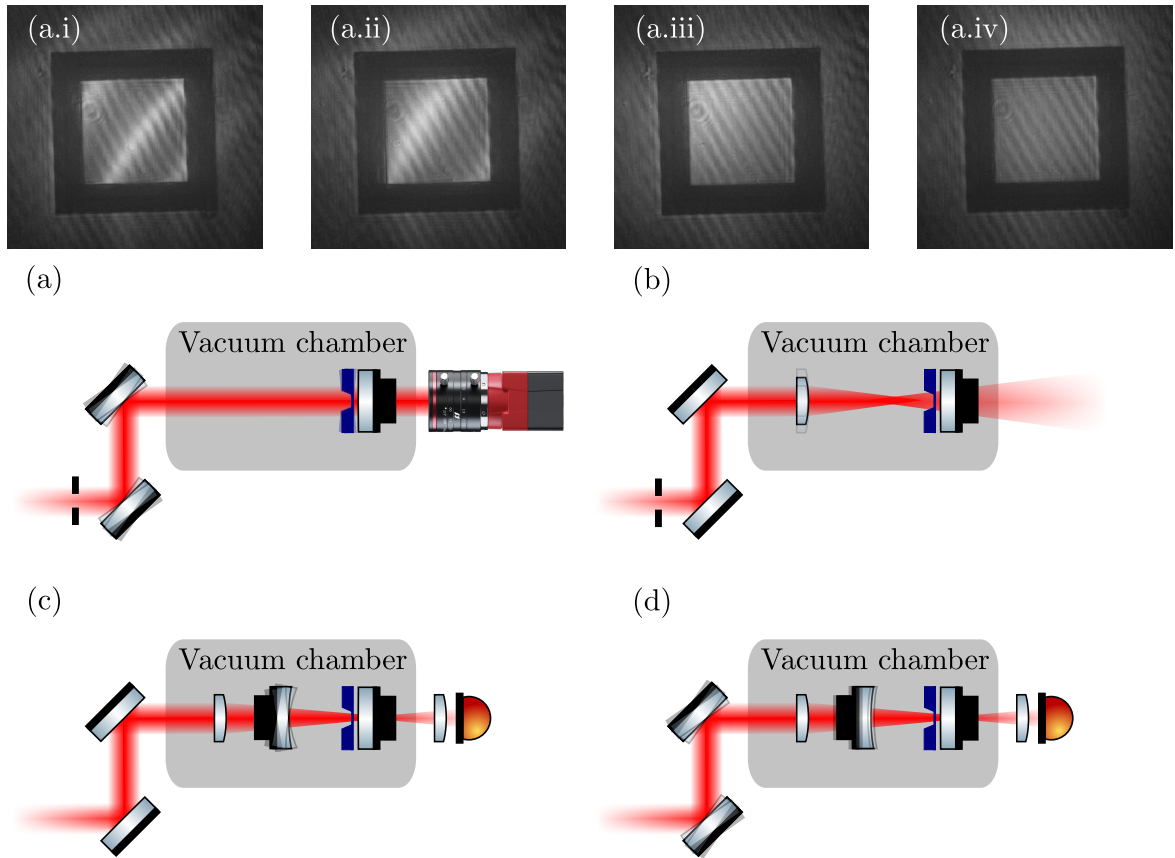


Fig. I.8 Set up alignment procedure. (a) to (d) show the steps to align the cavity with respect to the optical path (detailed in the main text). The (a.i) to (a.iv) show what is seen on the camera for four different tilt positions where (a.iv) displays a 'good' tilt alignment: no visible fringes except for the dim fringes of the camera setup. These dim fringes are present when the beam is a normal incidence with the back mirror (use of the iris) and are believed to be interferences arising from reflections inside the camera objective as they are seen whatever the plane of focus is.

key parameters of these two cavities are summarized in Table I.2. Both were mounted using 100ppm input mirrors, with a concave radius of curvature of -25mm, and a plane back mirror with a nominal transmission of 20ppm. Cavity I used the in-house fabricated membrane of nominal thickness 100nm, while cavity II used the commercial Norcada membrane of nominal thickness 50nm. The reason why we used the 100ppm input mirror rather than the 50ppm one was to ensure that the cavity linewidth would be larger than the mechanical resonance frequency of the membrane, such that we would be in the genuine unresolved sideband regime. Had we chosen the 50ppm mirror, the cavity linewidth would have been around 85kHz, an order of magnitude below the expected fundamental mechanical resonance

frequency of the membrane at 861kHz (see above). A tradeoff is to be made here, as using a higher transmission input mirror reduces the intracavity power for a given input power, thus reducing radiation pressure effects.

	Cavity I	Cavity II
Input mirror RoC (mm)	-25	
Back mirror RoC (mm)	∞	
Nominal input mirror T_1 (ppm)	100	
Nominal back mirror T_2 (ppm)	20	
Length L (mm)	17	24
FSR (GHz)	8.817	6.246

Table I.2: Summary of relevant parameters for the two cavities used in this work.

Cavity resonances versus membrane position

We first scan the input mirror piezo with a linear ramp V_{SW} ranging from 0 to 500V at 10-50Hz, corresponding to a displacements of around $2\mu\text{m}$ (~ 4 FSRs). The back piezo actuating the membrane position was driven by a DC voltage V_{DC} ranging from 0 to 70V, with an associated stroke of $4\mu\text{m}$ (3 piezos). Knowing the FSR of the cavity, we calibrate the piezo displacement as a function of the applied voltage, and fit the resonances positions using the theoretical model detailed in chapter 3. We modelled the front cavity length L_1 as well as the back cavity length L_2 as third order polynomials of the applied voltages V_{SW} and V_{DC} such that

$$\begin{aligned} L_1 &= a_0 + a_1 V_{\text{SW}} + a_2 V_{\text{SW}}^2 + a_3 V_{\text{SW}}^3 - \alpha V_{\text{DC}} \\ L_2 &= b_0 + b_1 V_{\text{DC}} + b_2 V_{\text{DC}}^2 + b_3 V_{\text{DC}}^3 \end{aligned} \quad (\text{I.2})$$

where we introduced the coefficients a_i and b_i to be fitted, as well as a cross-coupling term αV_{DC} to take into account the fact that the back piezo actuators does change the front cavity length since the piezo pushing the back cavity assembly bends the silicon frame.

We show a typical raw scan in Fig. I.9(a), as well as a rescaled one in Fig. I.9(b), where we can see a good agreement between the experimental data and the theoretical model. This fits allow us to extract the membrane reflectivity $|r_m|$, from which we can compute the power reflectivity and transmittivity of the membrane. This would tend towards using the single mode model as to describe radiation pressure in such a system.

Using (??) we can then estimate the membrane thickness to a surprisingly high accuracy with an error of less than 1nm. For cavity I, we found a thickness of $d = 86.9$ nm, while for

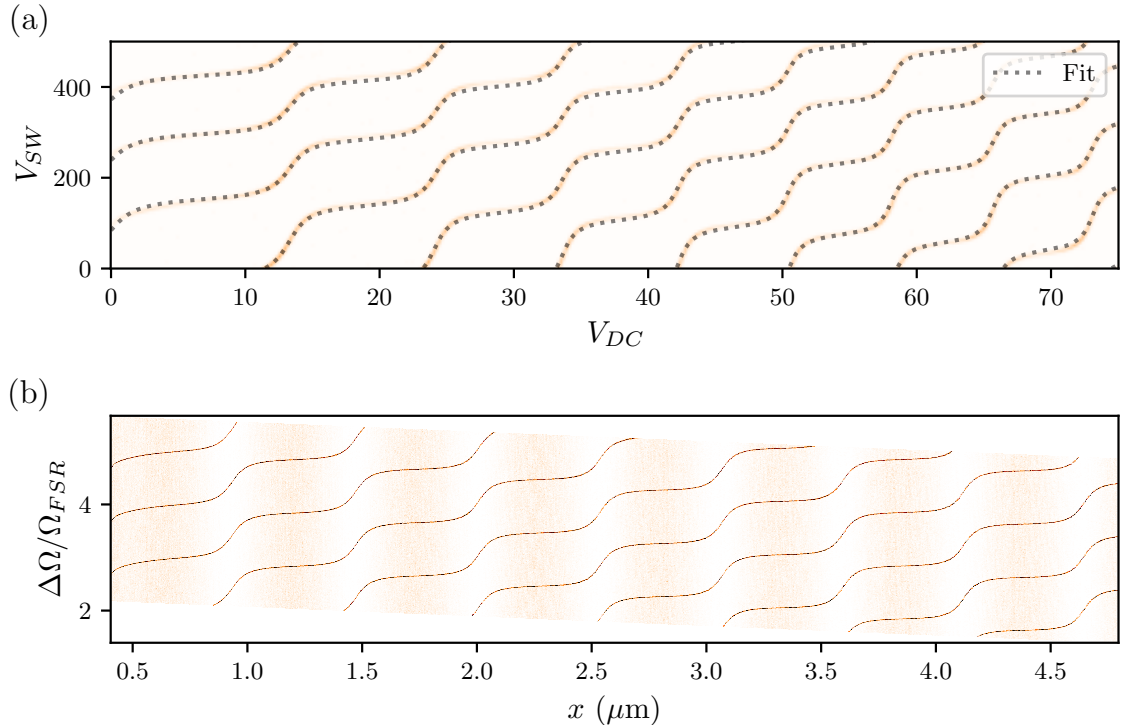


Fig. I.9 Scans of cavity I over few FSRs. (a) Raw scan of the cavity transmission as a function of the applied voltage V_{SW} on the front piezo and V_{DC} on the back piezo. The dashed line displays the theoretical model using the fitted membrane reflectivity $|r_m|$. (b) Rescaled scan where the fitted polynomials are used to convert the sweep voltage into effective cavity detuning in FSR unit, and the DC voltage into effective membrane displacement in microns.

cavity II we found $d = 41.1\text{nm}$ nm. For cavity I, the discrepancy with the nominal thickness of 100nm could be explained by the fabrication process used to make the membrane, i.e. the HF cleaning step at the end of the fabrication procedure etches the SiN layer at a rate of around 1nm/s. The membrane was cleaned for around 5 minute, such that we expected a thickness of around 90nm (it etches both sides of the membrane). For cavity II, the nominal thickness was 50nm, such that the discrepancy could be explained by fabrication tolerances.

From the fitted polynomials, we then extract the transfer functions of both piezo actuators, such that each measured observable can be mapped to an effective membrane displacement x rather than the applied voltages V_{SW} and V_{DC} . This gives us a displacement map shown in Fig. I.10, where we can extract the cavity length variations $\Delta L = \Delta L_1(V_{SW}, V_{DC}) + \Delta L_2(V_{DC})$.

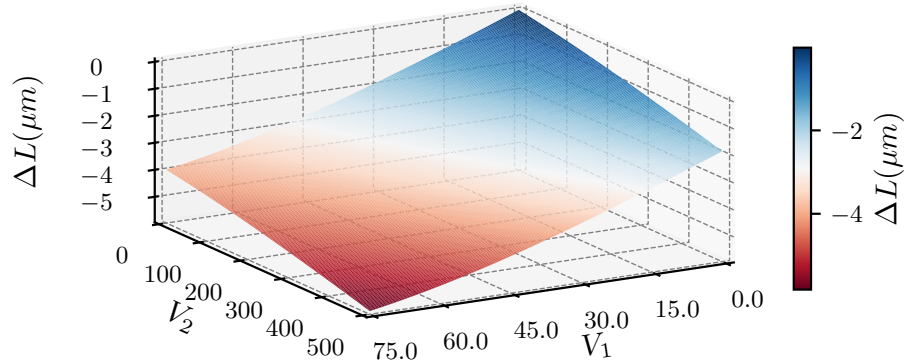


Fig. I.10 *Displacement map of cavity I.* Using the fitted polynomials, we can convert the applied voltages V_{SW} and V_{DC} into effective displacements of the membrane with respect to the back mirror. The colormap shows the total cavity length variations $\Delta L = \Delta L_1 + \Delta L_2$ as a function of both piezo voltages.

Importantly, we see that, contrary to the model developed earlier, the back piezo actuation does change the front cavity length, with a non zero coupling coefficient α . This is expected from the flexure tuning mechanism, where pushing on the back of the assembly bends the silicon frame, thus shortening the overall cavity length. Knowing these ΔL s variations, a natural next step would be to compensate the action of the back piezo on the long cavity length by adding a DC component to the front piezo voltage, such that the overall cavity length remains constant when tuning the membrane position. This would allow for a better decoupling of the membrane position and the cavity length, which would be useful for various experiments.

Slow and Fast Scans

As developed in ??, scanning over a cavity resonance can be done in two different regimes, depending on the sweep rate of the cavity length with respect to the cavity linewidth. In the adiabatic limit where the sweep rate is much smaller than the cavity linewidth, the intra-cavity field adiabatically follows the input field, and the transmitted and reflected intensities follow lorentzian lineshapes. In the opposite limit where the sweep rate is much larger than the cavity linewidth, dynamical effects such as cavity ringdowns appear, where the intra-

cavity field undergoes damped oscillations as the cavity length is swept over the resonance. This effect is visible both in transmission and reflection, as shown in Fig. I.11. This effect can be used to extract the cavity linewidth/finesse by comparing the heights of the first two rebounds in transmission to their temporal spacings, as detailed in chapter I. We will come back to this point later, particularly regarding the accuracy of the finesse estimation.

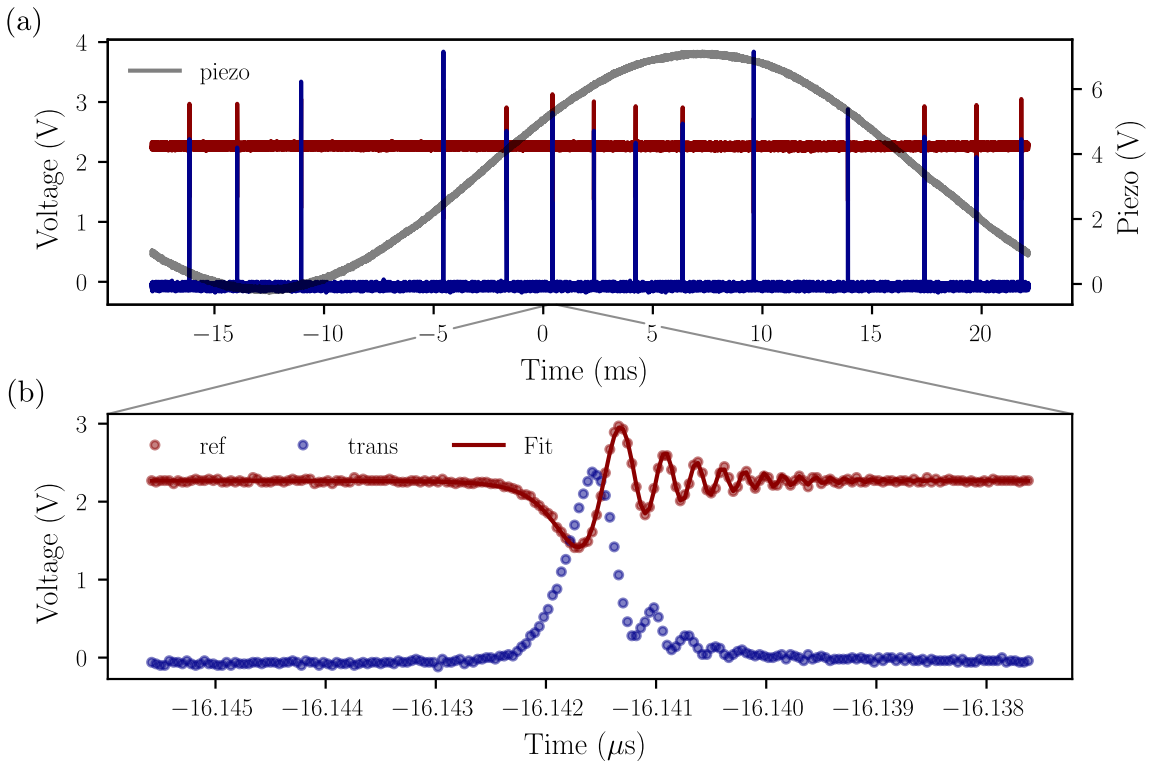


Fig. I.11 Larges cavity scans of cavity II showing dynamical effects such as cavity ringdowns both in transmission and reflection. The sweep rate is much larger than the cavity linewidth, such that the intracavity field cannot adiabatically follow the input field. (a) Cavity transmission and reflection swept over few FSRs. The blue curve (transmission) is eventually a single column of the 2D color plots showing the cavity scan in Fig. I.9(a). One can then actuate the back piezo to scan the membrane position as to see the cavity resonances shift. (b) Zoom on a single resonance showing cavity ringdown effects, with the fits used to compute the cavity linewidth and finesse.

To recover the lorentzian lineshapes, we first proceeded to apply slower sweep rates at the mHz level. This rendered the cavity sensitive to acoustic noise from the environment (the turbo pump for example), which did not yield quality lorentzian dips. We therefore kept the sweep rates at the 10-50Hz level, but drastically reduced the sweep amplitude to scan over a single resonance only. The classical EOM phase modulation sidebands is

then used as a frequency reference to extract the cavity linewidth, as shown in Fig. I.12 with a modulation frequency of 10 MHz. Having access to both transmitted and reflected intensities, and calibrating properly the photodiode response, we then have access to the η_T and η_R outcoupling coefficients defined in chapter 3.

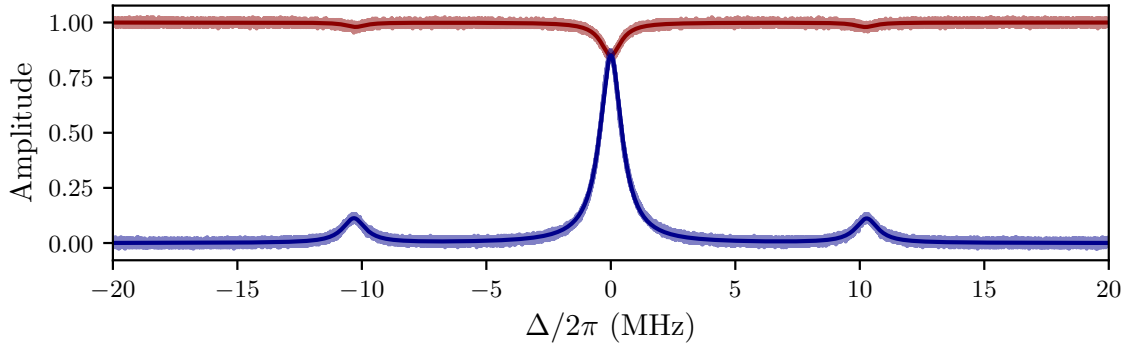


Fig. I.12 Small amplitude scan of cavity II over a single resonance (with membrane mounted), showing the transmitted and reflected intensities as well as the EOM sidebands used as a frequency reference to extract the cavity linewidth. The modulation frequency is set to 10 MHz. The fits (solid lines) are used to extract the cavity linewidth and finesse.

Finesse

We now turn to the evaluation of the system's finesse as a function of the membrane displacement. We use two different methods to evaluate the finesse of the cavity and we compare them:

- The first method would be to scan the cavity over a single resonance, and use the EOM sidebands as a frequency reference to extract the linewidth of the resonance. This method is less sensitive to piezo nonlinearities, assuming the piezo sweep is quasi linear over the resonance width.
- The second method would be to scan the cavity rapidly and observe a cavity ringdown, and compare the heights of the first two rebounds in transmission to their temporal spacings. This method is less sensitive to piezo nonlinearities, but requires a fast photodiode. Additionally we can vary the piezo sweep frequency to scan for various sweep rates and use a sine wave to sweep the cavity length such that the sweep rate is maximum at the sine zero crossing.

We then evaluate the finesse of the empty cavity as well as the cavity with the membrane inserted, at various membrane positions. This allows for an evaluation of the losses

introduced by the membrane insertion, as well as their position dependence i.e. position dependent linewidths/finesse. Assuming low scattering losses and absorption as reported in the literature for high-stress SiN membranes[SiN_review], we can attribute these excess losses to imperfect membrane alignment, i.e. remaining tilt between the membrane plane and the back mirror plane, imperfect mode matching to the cavity mode, and clipping loss due to the finite size of the membrane. The latter is not thought to be significant given the large size of the membrane with respect to the cavity mode waist, but could still contribute to few percents of the total losses.

The second method to estimate the cavity finesse turned out to be slightly disappointing, as it didn't yield consistent and reproducible results. Furthermore, numerical integration as to fit the measured data produces divergences (due to a low number of data points), which in turn forbids a proper estimation of the finesse. The reliable method was therefore taken to be the sideband method. A typical linear regression (detailed in Chap II) is still shown as an example in Fig. I.13, but the results shown in Fig. I.14 are only extracted from the sideband method.

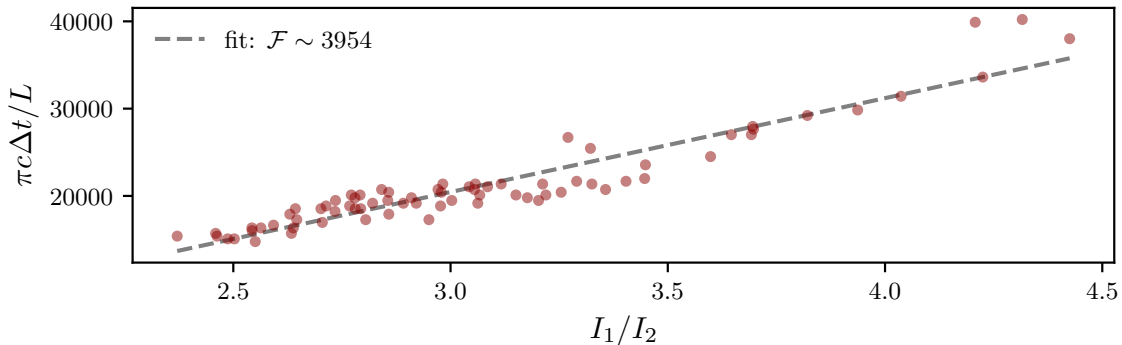


Fig. I.13 *Finesse measurement of cavity II using the ringdwon method. The data points show a typical linear regression used to extract the cavity finesse from the heights of the first two rebounds in transmission as a function of their temporal spacing.*

The results from the first method are shown in Fig. I.14, where we can see a good qualitative agreement with the theoretical model developped in chapter III. While cavity I featured an empty cavity finesse of 14 000, the insertion of the membrane reduced it to values ranging from 6 000 to 10 000 depending on the membrane position. Cavity II featured a lower empty cavity finesse of 12 780, which was further reduced to values ranging from 3 000 to 5 000 with the membrane inserted. These values are in line with other MIM/MATE systems reported in the literature[13, 12, 14], and could be improved by better membrane

alignment (tilt and transverse position).

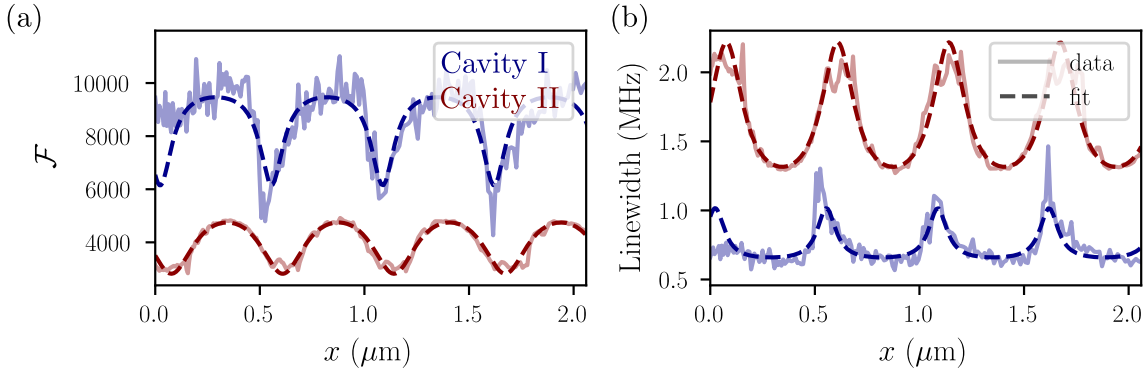


Fig. I.14 *Finesse measurement of the two cavities using the sideband method (a) and the associated linewidths (b). The finesse model in (??) has been changed as to account for the linear shifts underwent by all resonances as a consequence of the cavity shortening.*

Cavity outcouplings

Monitoring the cavity transmission while scanning over resonances with the input piezo allows us to extract the transmission and reflections dips of the cavity at a given position (calibrated using the scans). We then fit these position dependent outcoupling transmittivities using the model developed in chapter III. The resulting scans for both cavities are shown in Fig ...

Interestingly, the second cavity displayed anomalous dips, seen as abrupt changes in the transmittivities. These have been reported years ago in Jack Harris lab [ref], and occur when two optical modes become degenerate at a given membrane position. This was verified experimentally, as the mode matching was de facto less qualitative in the second cavity than in the first one.

Dispersive couplings

The next essential parameters central to MATE systems are the linear and quadratic dispersive couplings, as developed in chapter II. These are computed from the rescaled scans of the cavity resonances, giving access to the first and second derivative of the peak positions (once rescaled, expressed in FSR units) with respect to the membrane position. These are plotted in Fig I.16, and we see that, although the second cavity featured a lower finesse, it does display a larger linear dispersive coupling, ranging from ~ 20 to 90 GHz/ μm . These

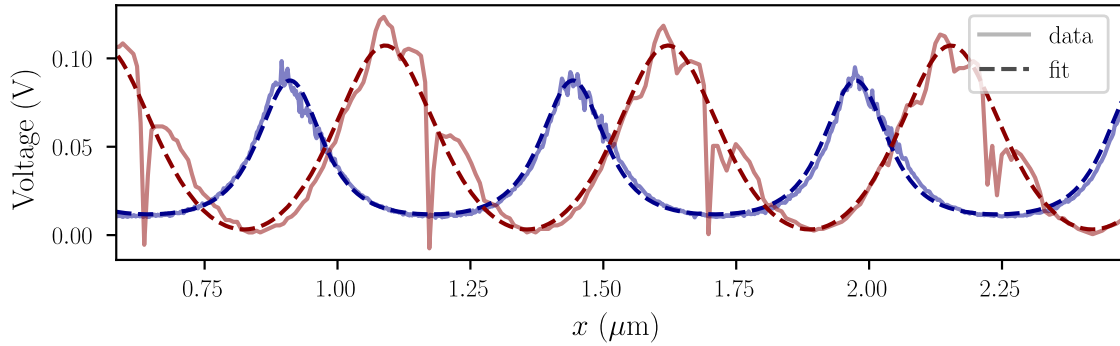


Fig. I.15 Transmission outcoupling coefficients η_T extracted from the fits of the cavity resonances for both cavities I and II as a function of the membrane position.

were observed to vary greatly from one cavity to another, independently of the cavity finesse.

From these various characterization sequences, we extract the key parameters of the two cavities, summarized in Table I.4.

Empty cavity	Cavity I	Cavity II
FSR (GHz)	8.817	6.246
Finesse \mathcal{F}	14 000	12 780
Linewidth (kHz)	630	489
$T_1 + T_2 + \mathcal{L}$ (ppm)	449	492
Resonant reflection R(0)	0.76	0.85
T_1 (ppm)	421	472
$T_2 + \mathcal{L}$ (ppm)	28	19
<hr/>		
MATE cavity		
Fitted reflectivity $ r_m $	0.54	0.33
Finesse \mathcal{F}	6 000 - 10 000	3 000 - 5 000
Linewidth (MHz)	0.88 - 2.20	1.25 - 2.10
$T_1 + T_2 + \mathcal{L}_{\text{mem}}$ (ppm)	630 - 1570	1255 - 2095
Input power	$10\mu\text{W} - 50\text{ mW}$	

Table I.3: Summary of the measured parameters for the two cavities used in this work.

I.2.2 Cavity Locking and Mechanical Characterization

Once the cavity was characterized, we proceeded to lock it using the PDH technique detailed in chapter III. The whole lock was done using PyRPL, as to showcase its versatility and ease of use. The analogic signal was manipulated with standard MiniCircuits® RF components, as to amplify/filter/mix the signals as needed. The overall locking sequence is shown in

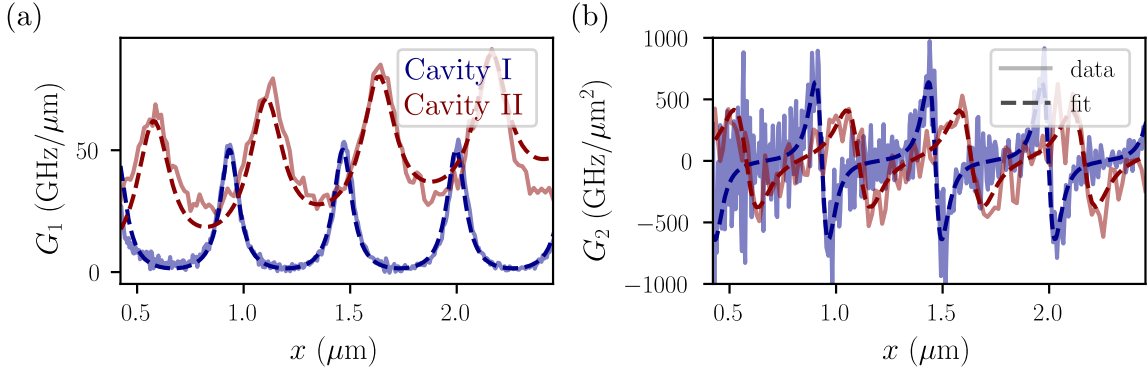


Fig. I.16 *Linear and quadratic dispersive couplings extracted from the rescaled scans of cavity I and II. Units are given in GHz/μm for G_1 and in GHz/μm² for G_2 , as rescaling by the zero point fluctuation in a cavity with a large number of photon obscures the true meaning of the vacuum optomechanical couplings. It is nonetheless discussed in the main text.*

Fig. I.17, where we can see the various steps needed to lock the cavity. First, performing a fine scan over a cavity resonance as to recover a lorentzian lineshape. From this, we tune the error signal amplitude and demodulation phase as to optimize the PDH error signal (Fig I.17(b)). We then engage the lock by first locking on the side of the resonance dip. It was observed that at mW powers, locking on the blue side of the resonance was not feasible. This could be explained by optomechanical heating of the membrane, as changing the side of the lock to the red side made the lock stable. Finally, we engage the PDH lock to lock onto the cavity resonance. The critical point in maintaining the lock was the input power i.e. the cavity circulating power. In terms of power range, locking at 1-50 μW held the lock, while ramping the input power to 1-50 mW greatly perturbed the optomechanical system such that it was no possible to keep the lock. We suspect that optomechanical heating, bistability and photothermal effects were playing a significant role in the lock stability.

Keeping the optical power low, the lock held, and we could proceed to the mechanical characterization of the membrane resonator. Using a spectrum analyzer (Agilent 90A20???), we monitored the spectrum of both the reflected intensity. The membrane motion modulating the cavity resonance faster than the lock could respond, the membrane motion modulates the intracavity field intensity, which can in turn be detected in direct detection in both transmission and reflection. The resulting spectra are shown for cavity II in Fig. I.18, where we can see the fundamental mechanical resonance at 861kHz, as well as various higher order modes. To reduce the averaging time, we used a Resolution Bandwidth (RBW) of 1kHz, which broadens the mechanical peaks, masking the true linewidth from which we could have extracted the effective mechanical quality factor.

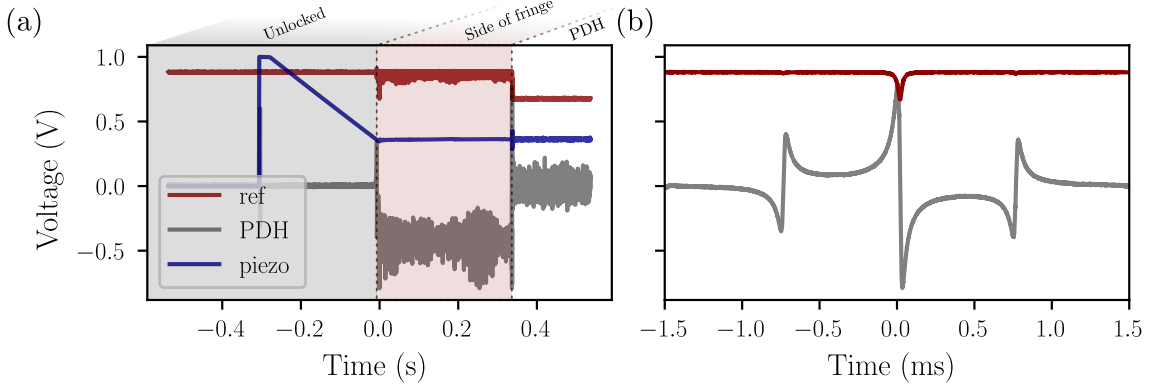


Fig. I.17 *Lock sequence of the MATE cavity using the PDH technique. (a)* Steps of the lock sequence, where we launch the side of fringe lock at approximately -0.3s. The red pitaya then sets its output voltage to 1 and starts PID control as to lock on the 0 of the error signal, which is achieved at time 0s. Being locked at a HWHM from resonance, launching the PDH lock then brings the cavity to resonance at time ~ 0.35 s. *(b)* Zoom on the error signal and reflected intensity during the lock sequence upon prior cavity scan. These traces are used to fine tune the error signal amplitude and demodulation phase as to optimize the PDH error signal.

To extract the intrinsic mechanical quality factor, we then proceeded to do mechanical ringdown measurements. Knowing the mechanical resonance frequencies from the spectra, we drive the membrane fundamental mode using the back mirror piezo, while sweeping the cavity. Recording the reflected intensity while triggering the oscilloscope on the piezo sweep

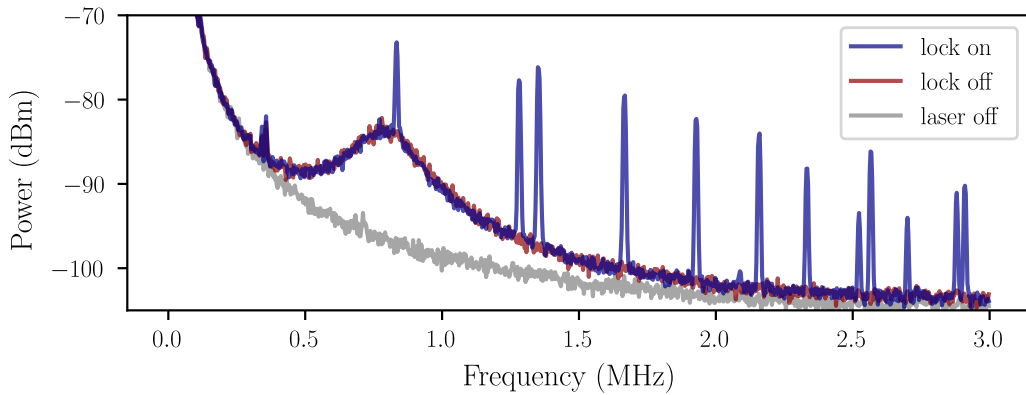


Fig. I.18 *Reflection mechanical spectrum of cavity II, showing the fundamental mechanical resonance at 861kHz as well as various higher order modes. We observe the relaxation oscillation peak at around 1MHz, as well as the laser technical noise at low frequencies. The RBW is set to 1kHz, which broadens the mechanical peaks and masks the mechanical linewidth.*

of the first mirror then yields the mechanical ringdown as shown in Fig. I.19(a), where each column of the image corresponds to a scope acquisition. The ringup phase is visible as the red area before time zero, where the piezo drives the membrane at resonance. At time zero, the piezo drive is stopped, and the mechanical motion decays exponentially with a characteristic time related to the intrinsic mechanical quality factor. By fitting the width of these decays, we can extract the mechanical quality factor as shown in Fig. I.19(b). For cavity II, we found a mechanical quality factor of $Q = 12000$, which is lower than expected from the nominal values given by Norcada (around 1 million).

The probable cause for this low mechanical quality factor is the stress applied to the membrane by the flexure mechanism. While this stress is necessary to tune the membrane position, it does reduce the mechanical quality factor by introducing additional loss channels such as clamping losses and internal friction due to bending of the membrane. This Q degradation was reported in MIM systems by Cindy Regal and coworkers, where they observed a drop from 10^6 down to 10^4 when the membrane frame was glued, adding stress to the membrane [15]. Therefore, while the flexure mechanism is necessary to tune the membrane position, it does degrade significantly the mechanical quality factor, which could be an issue for experiments requiring high Q_m such as ground state cooling or quantum limited measurements.

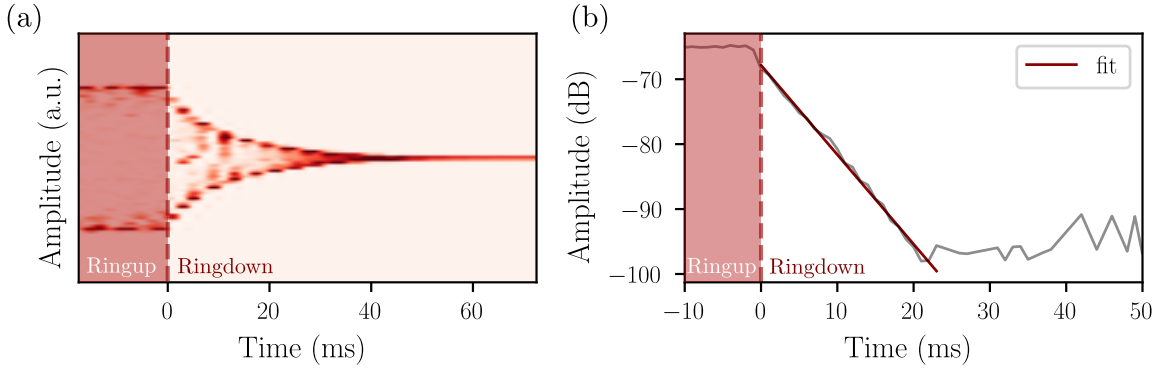


Fig. I.19 *Ringdown sequence of the fundamental mechanical mode of cavity II. (a) 2D colormap showing the mechanical ringdown as a function of time and acquisition number. Each column corresponds to a single oscilloscope acquisition triggered on the piezo drive stopping at time 0s. The red area before time zero shows the ringup phase where the piezo drives the membrane at resonance, while after time zero the mechanical motion decays exponentially. (b) Fit of the mechanical ringdown decay used to extract the intrinsic mechanical quality factor Q_m . From this fit, we found $Q_m = 12000$ for cavity II.*

I.2.3 Bistability

While characterizing the mechanical properties of cavity II, we observed an interesting bistability effect when driving the membrane at high optical powers (above 10mW input power). As shown in Fig. I.20(a), when sweeping the resonance using the front piezo, we observed a hysteresis depending on the sweep direction. This effect is reminiscent of bistability, where photo-thermal effects or radiation pressure effects induce a shift of the cavity resonance depending on the intracavity power.

The hysteretic response observed at high input power is characteristic of an optical nonlinearity that shifts the cavity resonance proportionally to the intracavity field. In the usual optomechanical (radiation-pressure) bistability, the resonance shift is mediated by the instantaneous displacement induced by the optical force, so the nonlinearity is essentially set by the mechanical susceptibility and reacts on mechanical time scales. By contrast, photothermal bistability originates from residual absorption: intracavity power heats the membrane/coatings, leading to thermo-refractive and/or thermo-elastic changes that detune the cavity; because the temperature follows the absorbed power with a finite thermal relaxation time, the detuning acquires a delayed component, which naturally produces sweep-direction-dependent hysteresis and can also enable dynamical backaction via this phase lag (as emphasized in photothermally induced transparency experiments). In our case, the appearance of the effect only above a clear power threshold, together with the strong hysteresis and the concomitant self-sustained oscillation consistent with a delayed force, points to a thermally mediated mechanism: a fraction of the intracavity power is absorbed by the membrane, heating it and shifting its effective position/optical response, thereby shifting the cavity resonance. We therefore attribute the bistability primarily to photothermal effects rather than to pure radiation pressure. The oscillation then sits precisely at the fundamental mode frequency, where a zoom can be seen in the inset of Fig. I.20(a), and the associated FFT spectra are shown for both sweep directions in Fig. I.20(b).

Unfortunately, due to time constraints (and membrane breakage...), we could not further investigate this interesting phenomenon, which would require a more in-depth study of the photothermal properties of the membrane, as well as the dynamical backaction effects at play in this regime. This would be an interesting avenue for future research, as photothermal effects can be harnessed for various applications such as cooling or amplification of mechanical motion, as well as for studying nonlinear dynamics in optomechanical systems.

I.2.4 Discussion & Perspectives

phononic crystals and ringdown from Patange to put here

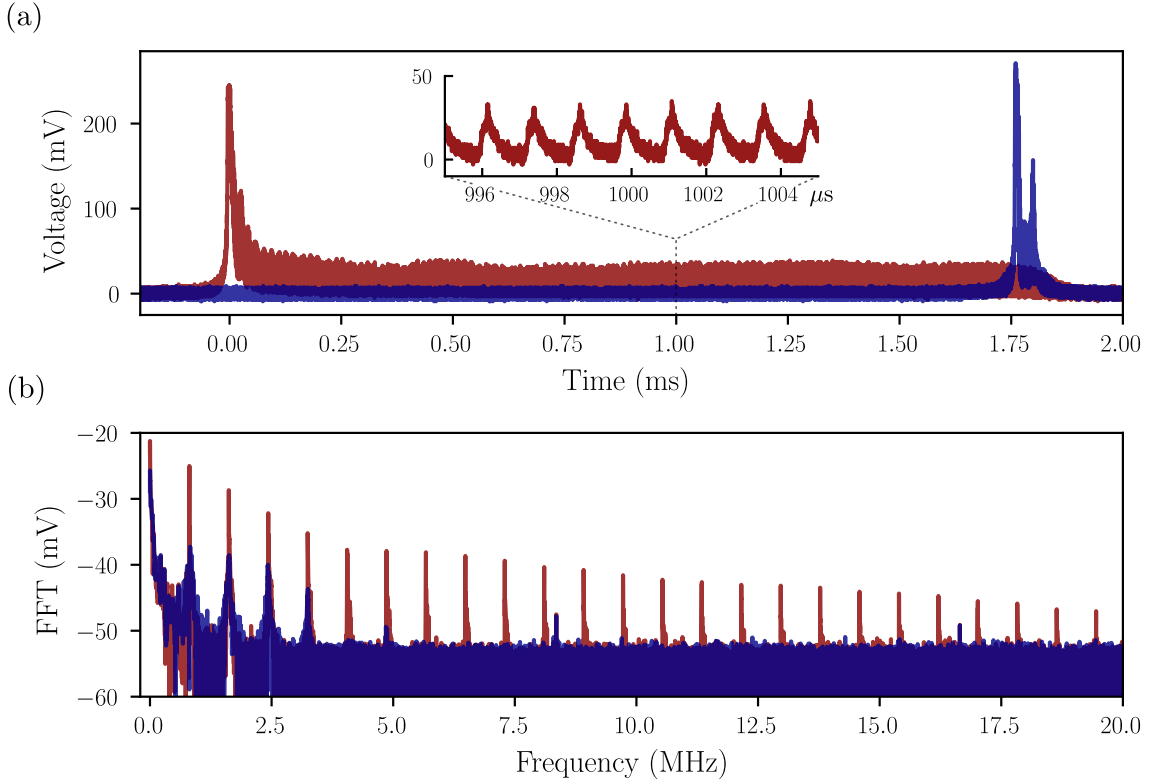


Fig. I.20 *Bistable behavior observed in cavity II at high input power ($> 10\text{mW}$).* (a) *Cavity transmission as a function of the front piezo voltage, showing a hysteresis depending on the sweep direction (blue: increasing voltage, orange: decreasing voltage).* The inset shows a zoom on the oscillations observed at the mechanical resonance frequency. (b) *FFT spectra of the transmitted intensity showing a peak at the fundamental mechanical resonance frequency and its harmonics, indicating self-sustained oscillations of the membrane motion.*

From these characterization sequences, we now compare the present system to previous systems used in the lab, as well as similar MIM/MATE systems reported in the literature to discuss its potential for future optomechanical experiments and motivate the next steps towards a fibered MATE cavity. Contrary to the systems historically studied in the group i.e. text-book FP cavities with an moving end mirror, the MATE system provides tunability of the optomechanical couplings, and benefits from sliting the high-Q mechanical resonator issue from the high-finesse cavity one. The mechanical resonator used here features exceptional mechanical properties, notably looking at its theoretical femtometer zero-point motion. To enhance radiation pressure effects, we want to maximize the linear and quartic dispersive couplings G_1 and G_2 , as well as the x_{ZPF} , the vacuum optomechanical couplings being the product of both. The figures of merit for radiation pressure effects are therefore the vacuum optomechanical coupling rates $g_0^{(1)} \propto G_1 x_{\text{ZPF}}$ and $g_0^{(2)} \propto G_2 x_{\text{ZPF}}^2$. These couplings are also

proportional to the membrane reflectivity $|r_m|$ and by the displacement-optical overlap ξ such that the effective vacuum couplings read $g_0^{(1)} \sim |r_m|\xi G_1 x_{\text{ZPF}}$ and $g_0^{(2)} \sim |r_m|\xi G_2 x_{\text{ZPF}}^2$ [Saarinen:23, 16]. In the following, we will assume perfect overlap $\xi = 1$ for simplicity, and we will use the 0.5 reflectivity membrane used in cavity I as a benchmark. We stress that a proper measurement of the vacuum optomechanical couplings would require a calibration of the membrane displacement spectrum, and a proper measurement/simulation of the mechanical mode effective mass, which was not performed in this work. Therefore, we will only discuss the anticipated vacuum optomechanical couplings based on the measured linear dispersive couplings and the nominal mechanical properties of the membrane (colored values in the table). We summarize the key parameters of various experiments in Table I.4.

	m	$\Omega_m/2\pi$	Q	x_{ZPF}	$g_0^{(1)}/2\pi$	$g_0^{(2)}/2\pi$
LKB micropillars	30 μg	3.6 MHz	7×10^7	9 am	25 Hz	4×10^{-12} Hz
LKB wheel	100 μg	300 kHz	3×10^6	17 am	47 Hz	2×10^{-11} Hz
This work	10 ng	861 kHz	1.2×10^4	1 fm	0-45 Hz	$\pm 2.5 \times 10^{-7}$ Hz
Future work	-	-	$> 10^8$	1 fm	0-2 kHz	$\pm 6 \times 10^{-4}$ Hz
Kippenberg 2024 [17]	7 ng	1.16 MHz	1.8×10^8	1 fm	160 Hz	-
Schliesser 2023 [18]	200 pg	1.3 MHz	1.4×10^8	5.7 fm	2.3 kHz	-
Harris 2015 [19]	43 ng	705 kHz	5×10^6	0.5 fm	2.2 Hz	-

Table I.4: Comparison of the key parameters used in this work to previous optomechanical systems studied in the group. Values in black are measured, while values in blue are computed under the assumption of perfect overlap $\xi = 1$. The *effective* masses put in the table are taken from L. Neuhaus and R. Metzdorff PhD thesis, while the mass of the membrane used here is taken from the literature for similar membranes. For the future work row, we assume moving to a fibered cavity with a cavity length of 500 μm i.e. a

Overall, our system features a decent linear optomechanical coupling range of 0-100 GHz/ μm (see Fig. I.16), which is two order of magnitude smaller than sub-millimeter cavities studied in the group. On the other hand, the membrane mechanical properties make it up for the moderate linear coupling, yielding a similar anticipated vacuum optomechanical coupling $g_0^{(1)}$ of tens of Hz (where we made the optimistic assumption of perfect overlap). The advantage of such a system resides in its tunability, where one could put the system in a linear or quadratic coupling regime at will, or investigate dissipative coupling effects. Regarding MIM/MATE systems reported in the litterature, our centimetric system in a MATE configuration features promising couplings in comaprison to sub-mm MIM systems used to demonstrate quantum ground state cooling [18, 17], albeit with a lower mechanical quality factor.

To put this in perspective with the single ended cavity, we consider the parameters nec-

essary to reach similar estimated vacuum optomechanical couplings for our future work i.e. the kHz range, with realistic mechanical resonator/mirror i.e. $m \sim 10 \mu\text{g}$ and $\Omega_m/2\pi = 1 \text{ MHz}$, which gives $x_{\text{ZPF}} \sim 30 \text{ am}$. We set the cavity linewidth to $\kappa/2\pi > 100 \text{ MHz}$ to sit in the unresolved sideband regime, and we want to reach $g_0^{(1)}/2\pi \sim 1 \text{ kHz Hz}$, which eventually dictates what the cavity length should be for a 1064 nm IR beam. This gives us a cavity length of $L \sim 8 \mu\text{m}$, which is extremely demanding. Regarding the finesse, the bounds set on the cavity linewidth then yields a maximum finesse of about 2×10^5 , which is also very challenging to make (but it is a highest bound so it is fine). A standard cavity of finesse 10 000 would perfectly fit the needs, the main challenge being the cavity length. This simple calculation showcases the great properties of highly stressed SiN membranes, which allow to reach decent vacuum optomechanical couplings even in centimetric cavities. Furthermore, the SiN being a very handy material to do lithography with, this also explains the recent interest in patterning these membranes with both a phononic crystal (to enhance the mechanical quality factor) and a photonic crystal in its center (to enhance the reflectivity, and therefore the optomechanical couplings) such that this 10ng membrane genuinely behaves as a text-book optomechanical resonator [**Saarinen:23**, [16](#)].

Two natural avenues for improvement arise from this comparison. First, reducing the cavity length by two order of magnitude would naturally enhance the dispersive couplings by the same amount, yielding anticipated vacuum optomechanical couplings in the kHz range. This would require moving to a fibered cavity architecture, which is the next step of this project as detailed in the next section. Second, improving the mechanical quality factor by two order of magnitude (up to 10^6) would render this system competitive with state-of-the-art optomechanical systems used to demonstrate quantum ground state cooling and quantum limited measurements. This could be achieved by using phononic crystal patterned membranes, or by moving from the flexure-tuned design explored in this section. Finally, an easy way to get a two-fold increase of the vacuum optomechanical couplings would be to use a higher reflectivity membrane (for example a 0.9 reflectivity membrane would double the couplings).

I.3 Optomechanical Fibered Cavity

Having characterized the MATE cavity phenomenology, we now turn to the specifications, design and preliminary steps towards the realization of a fibered optomechanical cavity using a MATE architecture.

The reasons why one would want to build a micrometer/millimeter scale optomechanical

cavity are numerous. First, the small mode volume allows for a large optomechanical coupling rate g_0 , as the linear dispersive couplings scale as the inverse of the cavity length. Additionally, for a fixed finesse and a fixed resonator frequency of about 1MHz, the cavity linewidth κ becomes easily larger than the mechanical frequency, rendering the unresolved sideband regime easily achievable. One can then boost the finesse, enhancing radiation pressure effects while remaining in the unresolved sideband regime. Finally from an experimental point of view, it seems that free space cavities embedded within cryogenic environments tend to suffer from unwanted intensity and phase fluctuations, severe misalignment issues, and limited optical access. The beam being injected by and collected from AR coated windows, and the cryostat being subject to acoustic and vibrational noise from the environment (pumps, acoustics, etc), the cavity intracavity power fluctuates significantly, rendering stable locking and long term operation difficult. Fibered cavities, on the other hand, are more compact, easier to align and maintain aligned, and can be directly integrated within cryostats with minimal optical access requirements (only the fiber feedthroughs).

This work was carried out in collaboration with the group of **Jakob REICHEL** and **Romain LONG**, as well as with **Pierre MAHIOU** from the spin-off company Mirega, who I once again deeply thank for his patience, expertise and availability throughout our collaboration. **Amin LAKHAL**'PhD thesis will focus more extensively on this optomechanical experiment.

I.3.1 Design considerations

Moving to micrometric cavities imposes stringent design constraints, as the cavity length needs to be precisely controlled and tuned, and the radii of curvature of the fiber mirrors need to be chosen as to provide a stable optical resonator while minimizing losses, which would degrade the squeezing level coupled to the cavity mode. Additionally, the membrane needs to be mounted and aligned within the small cavity volume, which imposes further constraints on the membrane assembly size and actuation mechanisms.

Cavity mode & coupling efficiency

In a fibred Fabry–Perot operated at micrometric lengths, the spatial mode is set by the optical constraint that the cavity eigenmode at the input mirror must efficiently overlap with the guided mode exiting the injection fiber. We denoted the waist of the cavity as w_0 , and the guided mode radius of the fiber as w_0^f . We recall the waist size of the fundamental Gaussian mode in a plano-concave cavity,

$$w_0 = \sqrt{\frac{\lambda}{\pi} \sqrt{L(R - L)}},$$

where L is the cavity length and R the radius of curvature of the concave mirror. The waist as a function of the distance z from the waist reads

$$w_{\text{cav}}(z) = w_0 \sqrt{1 + \left(\frac{z}{z_R}\right)^2}, \quad z_R = \frac{\pi w_0^2}{\lambda}.$$

The coupling efficiency between the fiber mode and the cavity mode can be computed from the overlap integral between both modes, assuming perfect axial alignment and no tilt at the fiber–cavity interface [ref]. This yields the coupling efficiency

$$\epsilon \approx \frac{4}{\left(\frac{w_0^f}{w_0} + \frac{w_0}{w_0^f}\right)^2 + \frac{(z_0 - z_0^f)^2}{z_R z_R^f}}, \quad (\text{I.3})$$

where z_0 and z_0^f are the positions of the cavity waist and fiber waist respectively, and z_R and z_R^f their associated Rayleigh ranges. This expression shows that optimal coupling efficiency is obtained when both waists are matched in size and position, i.e. $w_0 = w_0^f$ and $z_0 = z_0^f$.

We then have two configurations to consider, as shown in Fig. I.21 i.e. injecting the light from the flat fiber mirror or from the curved fiber mirror. To realize the MATE system, the resonator needs to be positioned near the flat fiber interface. As seen in the coupling efficiency expression, setting $z_0 = z_0^f$ requires the cavity waist to be located at the flat mirror, which is naturally achieved in configuration A.

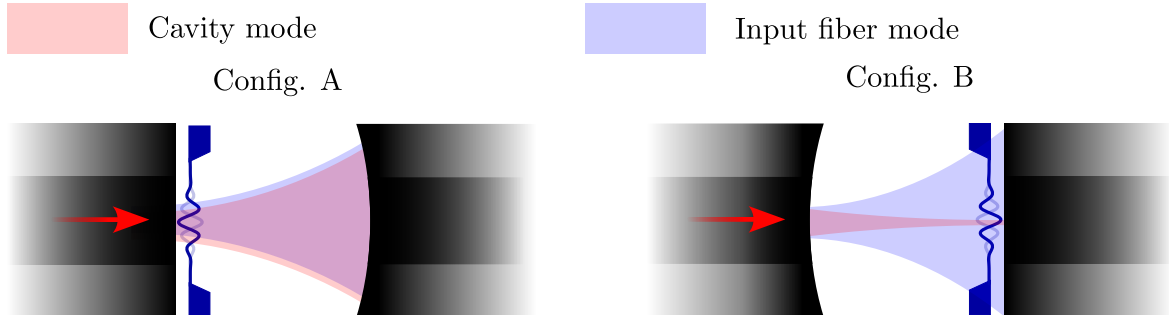


Fig. I.21 Two possible configurations for a fibered MATE cavity. (a) shows the configuration where the membrane is mounted on the input fiber mirror, while (b) shows the configuration where the membrane is mounted on the back mirror. The overlap between the cavity mode and the input fiber mode needs to be maximized as to ensure optimal mode matching to the cavity mode. The components are not to scale.

Choice of fibers

In order to couple a single fiber mode to the cavity mode, we need to select an appropriate fiber type. For injection, multi-mode (MM) fibers are not suitable, as the presence of higher order modes would lead to parasitic coupling to the cavity mode, reducing the effective coupling efficiency and leading to unwanted interference effects. Therefore, single mode (SM) fibers are the natural choice for this application. Hence, let's first consider a standard SM fiber at 1064nm, such as the Thorlabs SM-1060 XP. The specified mode field diameter is $6.2\mu\text{m}$, corresponding to a mode radius and cavity waist of $w_0^f = w_0 = 3.1 \mu\text{m}$. The associated Rayleigh range is $z_R = \pi w_0^2 / \lambda \approx 28.5 \mu\text{m}$, yielding feasible L and R values of the order of a few tens of microns. Embedding a membrane within such a short cavity length is however extremely challenging, since the Si membrane frames are typically few hundreds of microns thick. We would then need to mount the cavity around the membrane, which forbids to change the resonator at will.

In practice, this strongly motivates the use of *large mode area* (LMA) fibers for light injection: a larger mode field diameter $2w_0^f$ allows to increase the cavity waist w_0 , and therefore the Rayleigh range z_R , relaxing the constraints on the cavity length and mirror radius of curvature. This in turn allows to insert larger membrane assemblies within the cavity, while keeping the mode matching intact. A reference LMA fiber purchased by the lab is the Coherent LMA-GDF-20-125, featuring a core diameter of $20 \mu\text{m}$ and aperture of $\text{NA} \simeq 0.08$, whose specified values will be used here for simulations. The normalized frequency (V-number) of such a fiber reads

$$V = \frac{2\pi a}{\lambda} \text{NA}, \quad (\text{I.4})$$

which, at $\lambda = 1064 \text{ nm}$, gives $V \simeq 3.8$. This useful number approximates the number of modes a fiber can guide, making the LMA fiber a *few mode* fiber. The company however claims it is easily operated in single mode by properly adjusting the input coupling conditions and not constraining the fiber too tightly, or with critical bending radii. The corresponding fundamental guided-mode radius can be estimated from standard step-index formulae. Using the Marcuse-Petermann approximation,

$$w_P \simeq a \left(0.65 + \frac{1.619}{V^{3/2}} + \frac{2.879}{V^6} - \left(0.016 + 1.561 V^{-7} \right) \right), \quad (\text{I.5})$$

one obtains a mode radius $w_0^f \sim w_P \sim 8.5 \mu\text{m}$. This sets the target cavity mode size at the injection mirror for efficient coupling, i.e. $w_{\text{cav}}(z=0) \sim w_0^f$. The Rayleigh range $z_R \sim 2.2 \times 10^2 \mu\text{m}$ then gives us the order of magnitude of the cavity length and mirror radius of curvature needed to achieve good mode matching, which are now in the hundreds

of microns range, making the membrane insertion more feasible.

Regarding the collection fiber, we note that even if the injection is optimally mode-matched to the cavity waist using the LMA fiber (with $w_0^f \simeq w_0 \simeq 8.5 \mu\text{m}$), the cavity mode expands over the cavity length. Using $L \simeq 500 \mu\text{m}$ and $R \simeq 600 \mu\text{m}$ at 1064nm, the beam radius at the second mirror reaches $w(L) \approx w_0 \sqrt{1 + (L/z_R)^2} \simeq 22 \mu\text{m}$. In other words, the output mode is roughly a factor ~ 2.5 larger than the injected mode. As a result, collecting the transmitted light back into the same LMA fiber would incur a substantial mode-mismatch loss (even under perfect alignment), whereas a large-core collection fiber can capture essentially all of the emerging power without requiring tight matching to a single transverse mode. For this reason, while injection is conveniently performed using an LMA single-mode fiber, the collection will be implemented with a MM fiber.

Using the estimated mode field diameter of the LMA fiber, we can compute the coupling efficiency as a function of the cavity length and mirror radius of curvature, as shown in Fig. I.22(a) to seek for optimal cavity parameters. We observe a plateau of high coupling efficiency around the optimal condition, showing the robustness of the coupling to small deviations from the optimal geometry. Additionally, we plot in Fig. I.22(b) the coupling efficiency as a function of a variation in the mode field diameter of the fiber for $R = 600 \mu\text{m}$. This shows that a precise knowledge of the fiber mode field diameter is not critical to achieve good mode matching, as variations of hundreds of nanometers still yield coupling efficiencies above 90%, which would result in marginal losses in terms of squeezing level coupled to the cavity mode i.e. $\sim 0.5\text{dB}$.

Maintaining good mode matching also requires precise alignment of the fiber in the transverse plane, as well as controlling the tilt of the fiber mirror. The coupling efficiency as a function of a misalignment d in the transverse plane is given by [Siegman1986]

$$\epsilon(d) = \epsilon e^{-(d/d_e)^2}, \quad \text{with} \quad d_e^2 = \frac{2}{\epsilon((1/w_0^f)^2 + (1/w_0)^2)}. \quad (\text{I.6})$$

Similarly, the coupling efficiency as a function of a tilt misalignment θ between the fiber and the cavity mode reads [Siegman1986]

$$\epsilon(\theta) = \epsilon e^{-(\theta/\theta_e)^2}, \quad \text{with} \quad \theta_e^2 = \frac{2}{\pi^2 \epsilon ((w_0^f/\lambda)^2 + (w_0/\lambda)^2)} \quad (\text{I.7})$$

and the general coupling efficiency becomes $\epsilon(d, \theta) = \epsilon e^{-(d/d_e)^2} e^{-(\theta/\theta_e)^2}$. These two expressions are plotted in Fig. I.23(c) and (d), showing that the transverse positioning of the fiber should be precise to submicrometric precision to optimize the mode matching, while the tilt

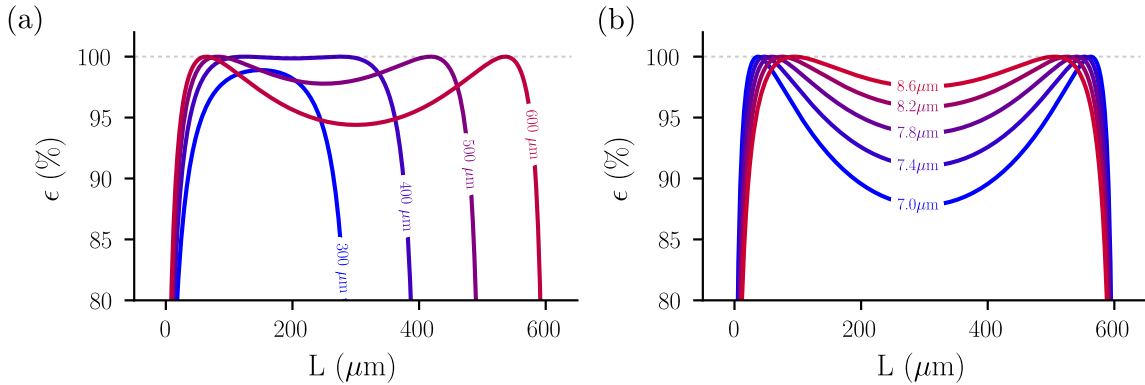


Fig. I.22 *Coupling efficiency of the fiber mode to the cavity mode as a function of various parameters. (a) Coupling efficiency as a function of the cavity length L and the mirror radius of curvature R . The dashed line shows the optimal coupling condition. We observe a plateau of high coupling efficiency around the optimal condition, showing the robustness of the coupling to small deviations from the optimal geometry. (b) Coupling efficiency as a function of a variation in the mode field diameter of the fiber for $R=600\mu\text{m}$.*

should be controlled to within few mrad. These constraints are achievable using standard fiber positioning stages such as NanoMax® stages from Thorlabs.

I.3.2 Fiber mirror fabrication

The fabrication of high quality fiber mirrors is a crucial step in the realization of fibered optomechanical cavities. The mirrors need to feature low surface roughness, precise radii of curvature, and high reflectivities to achieve high finesse cavities. The fabrication process typically involves the following steps:

Fiber preparation: The optical fibers are first cleaved to obtain a clean and flat end face. This is typically done using a precision fiber cleaver to ensure a perpendicular cut.

Laser machining: The cleaved fiber end faces are then shaped using a CO₂ laser. By carefully controlling the laser parameters (power, duration, focus), we can create concave or flat profiles on the fiber tips. Single or multiple laser shots can be used to achieve the desired curvature and surface quality. The machined fiber tips are then characterized using interferometric profilometry to measure their surface profiles and ensure they meet the required specifications.

Coating deposition: After shaping, the fiber tips are coated with high-reflectivity dielec-

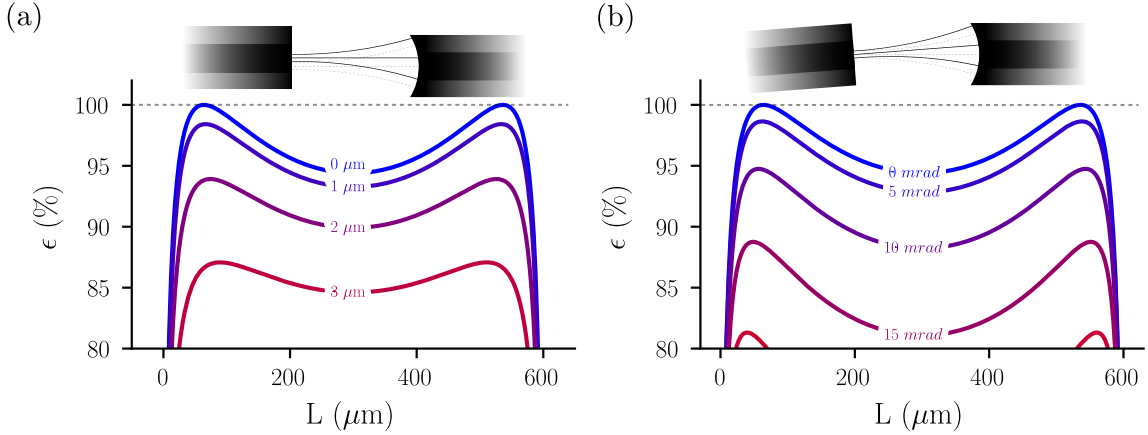


Fig. I.23 *Coupling efficiency of the fiber mode to the cavity mode as a function of various parameters. (b) Coupling efficiency as a function of a variation in the mode field diameter of the fiber for $R=600\mu\text{m}$. (c) Coupling efficiency as a function of a transverse misalignment between the fiber and the cavity mode for $R=600\mu\text{m}$. The positioning of the fiber should hence be precise to submicrometric precision to optimize the mode matching. (d) Coupling efficiency as a function of a tilt misalignment between the fiber and the cavity mode for $R=600\mu\text{m}$. The tilt should be controlled to within few mrad.*

tric coatings using techniques such as ion beam sputtering or electron beam evaporation. The coatings are designed to achieve the desired reflectivity at the operating wavelength.

Characterization: The reflectivity of the coatings are then to be measured using transmission measurements for a rough estimate. More precise measurements can be done by integrating the fiber mirrors into a test cavity and measuring the finesse and resonant reflectivity.

Over my PhD I only got to fabricate and characterize the fiber profiles, while the coating deposition and reflectivity measurements are to be taken over by **Amin LAKHAL** who designed a custom fiber holder with **Pierre MAHIOU** to coat the fibers at the LMA, following the same recipe briefly detailed earlier for the free space mirrors. There, and supervised by **Jerome DEGALLAIX** and **David HOFMAN**, he will need to develop a precise protocol to handle, clean, coat and characterize the fiber mirrors. The first trial of coating realised in 2025 was not successful.

The setup used to shape the fiber tips using the CO₂ laser is shown in Fig. I.24. The system combines external pulse generation and focusing optics with a high-precision three-axis translation platform for reproducible positioning i.e. shooting path, complemented by an optical profilometer for surface metrology i.e. imaging path. The entire setup is housed in

a temperature-stabilized enclosure, and includes a motorized tip/tilt stage to align the fiber facet perpendicular to the CO₂ beam prior to machining. The machining and profilometry beam paths are kept separate, allowing reliable shuttling between processing and measurement locations. The profilometry stage provides sub-micron lateral resolution and, through averaging, can reach sub-nanometer height sensitivity, enabling automated centering and alignment of fiber cores before fabrication.

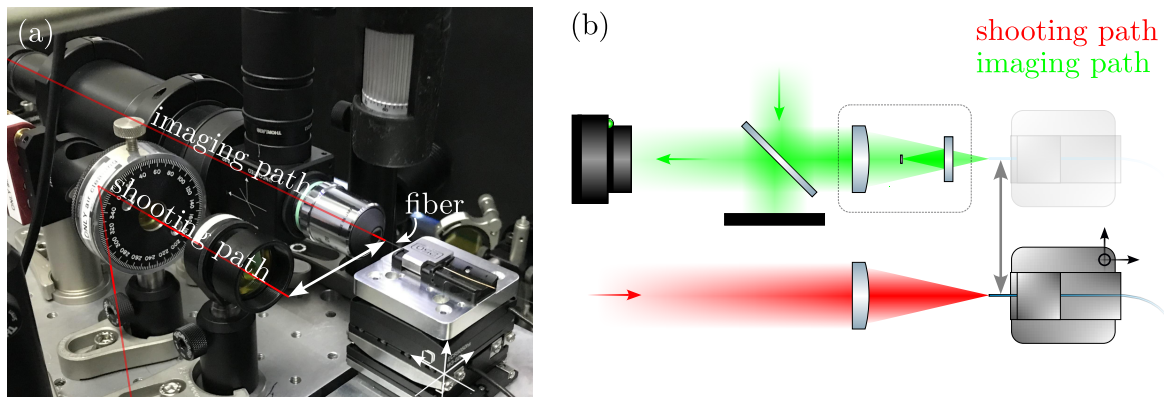


Fig. I.24 CO₂ laser machining setup for fiber mirror fabrication. (a) Picture of the setup, where we can see the CO₂ laser path, the imaging path, and the fiber mounted on a 3-axis translation stage. (b) Schematic of the setup, showing the CO₂ laser beam focused onto the cleaved fiber tip using a lens. The fiber is mounted on a 3-axis translation stage to allow precise positioning and focusing of the laser beam. The precision translation stages allow to move the fiber in and out of the laser focus as needed, implement multiple laser shoot routines, and go back and forth between imaging and machining. The imaging part uses a 515nm LED source along with a Mirau objective to reconstruct the fiber profile interferometrically.

Using this setup under supervision of **Pierre MAHIOU**, I helped fabricating and characterizing various fiber profiles, some of which are shown in Fig. I.25. We can see a flat fiber profile obtained after cleaving and *cleaning* the fiber tip using a defocused CO₂ laser shot to remove surface roughness (a). We also see two concave profiles obtained using single (b) and multiple (c) CO₂ laser shots, yielding parabolic profiles over the fiber core with radii of curvatures ranging from tens to hundreds of microns.

I.3.3 Designs and optical layout

Based on the design considerations detailed earlier, we can now propose various designs for the fibered MATE cavity. Additionally, and similarly to our free space MATE cavity, we need to make the system vacuum and cryo compatible, as to allow for low temperature op-

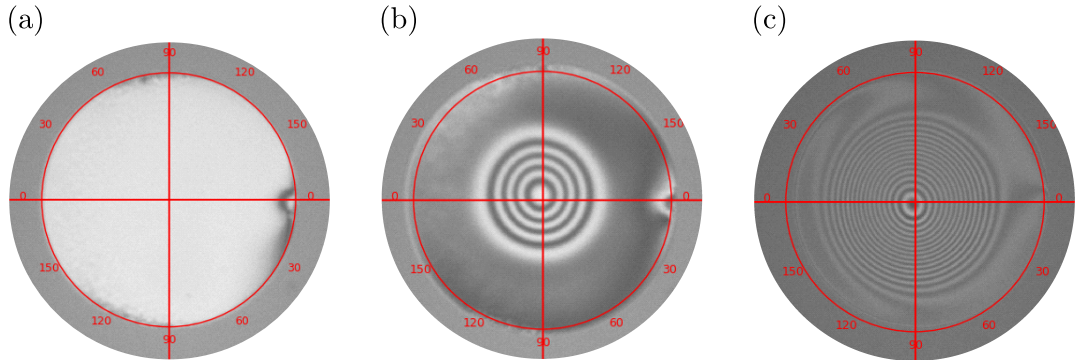


Fig. I.25 Interferometric readout of the fiber profiles using a LED at 515nm. Superposing the light field reflected of the fiber surface with a plane phase reference allows to reconstruct the fiber profile with nanometric accuracy. (a) Profile of a flat fiber, that could be used as a plane mirror. The fiber is cleaved and then cleant using a CO₂ laser to remove surface roughness. (b) Profile of a concave fiber mirror machined using a single shot of the CO₂ laser. The profile yields a gaussian shape. (c) Profile of a concave fiber mirror machined using multiple shots of the CO₂ laser, yielding a parabolic shape.

eration. This would point towards the same material as before i.e. OFHC copper, which can be gold coated to prevent oxidation and improve thermalization. The piezo actuators used to tune the cavity length should also be cryo compatible while allowing for sufficient stroke at low temperatures. The Noliac®NAC2402-H3.4 piezo actuators would seem to provide sufficient displacement at cryogenic temperatures i.e. $6\mu\text{m} \times 2 \times 20\% \sim 2.5 \mu \rightarrow 5 \text{ FSRs}$, where $6\mu\text{m}$ is the room temperature stroke, 2 for the two piezos, and 20% the expected displacement in bipolar operation at 10mK: they provide enough displacement as to lock the cavity on resonance with one piezo, and change the relative position of the membrane with respect to the second fiber mirror with the other.

The main challenge lies in inserting and aligning the membrane within the small cavity volume, while allowing for precise tuning of its position. The three main designs considered are shown in Fig. I.26, where we elaborated a ferrule-based and two v-groove based designs. We now detail their respective advantages and drawbacks.

Ferrule design (a) allows for a (relatively) easy alignment of the cavity mirrors using ferrules hosted within ferrule holders glued to the piezos. Like in Harris or Sankey's lab, a single *dummy* fiber would first be inserted through both ferrules/holders to provide a passive alignment. They can then be glued in place. Once the ferrule holders are glued, the dummy fiber is removed and replaced by the actual fiber mirrors. The membrane is then inserted

from the top of the assembly, and held in place using two fine screws, providing a mean to correct for tilt. Upon the dummy fiber removal, one would then need to insert the actual fiber mirrors without damaging them, which is challenging. It was reported that coatings on fiber tips usually thicken the fiber diameter by a few microns near the tip, which can prevent the fiber from being inserted fully into the ferrule, leading to breakage. Removing extra material from the fiber tip by chemical means is an active area of research in some labs, but no established protocol exists yet. As seen earlier in the chapter, constraining the membrane frame too much degrades the mechanical quality factor too.

V-groove design I (b) uses v-grooves to host the fiber mirrors, inspired by the fiber cavities developed in Jakob Reichel's group. The v-grooves are then held/glued by their sides using silica pieces, themselves glued on the piezo actuators. The alignment is carried out using a piezoelectric fiber gripper providing force-free release and fine translation, opposed to a tilt-mounted fiber holder for angular optimization. After maximizing the cavity coupling, UV-curable glue is applied to fill the groove/channel surrounding the fiber and is cured using a small-diameter UV beam to confine curing to the adhesive and mitigate drift. The process is repeated for the second fiber, and the final assembly is completed by adding local strain-relief points and minimizing the free-standing fiber length. The Reichel group has experience with this type of design, having used it to probe fiber cavities with record finesse. The membrane is again inserted from the top and held in place using two fine screws. This design still constrains the membrane frame.

V-groove design II (c) aims at preserving a higher mechanical quality factor by avoiding constraining the membrane frame too much. In this design, the membrane is glued/held onto a separate piece, which is then inserted from the top and screwed onto the cavity base plate. This allows for a more flexible mounting of the membrane, potentially preserving its mechanical quality factor better than the other designs. The cavity alignment and fiber mounting is similar to design (b).

It was then decided to proceed with the V-groove design II (c), as it seemed to provide the best compromise between ease of assembly, cavity alignment, and mechanical quality factor preservation. The final design is shown in Fig. I.27, where we can see the various components of the cavity assembly. The membrane is glued/kapton taped to the membrane holder, which is then screwed to the cavity base plate. This should avoid adding stress to the membrane frame. Attention should be paid to thermally anchor the fibers properly to the copper base plate, as to ensure good thermalization of the cavity mirrors at low temperatures.

Once the cavity aligned and the membrane inserted, both fibers are to be spliced *in-situ*

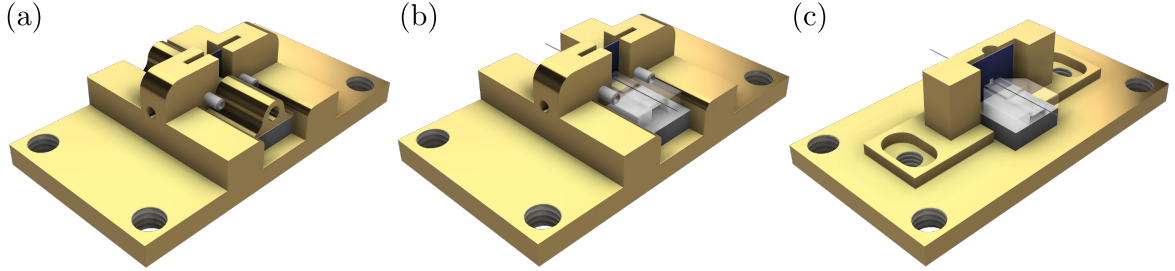


Fig. I.26 Examples are three possible designs for the fibered MATE cavity. (a) Ferrule based design, where the membrane is inserted from the top of the assembly, then held in place by two fine screws, and where the fibers are inserted inside ferrules. (b) V-groove based design, where the fibers are held and glued in v-grooves positioned on the piezo actuators. Similarly as in (a), the membrane is inserted from the top and held in place by two fine screws. (c) V-groove based design where the membrane is glued on a separate piece, then inserted from the top and screwed to the cavity base plate. This design avoids constraining the membrane frame too much, hence preserving a higher mechanical quality factor in theory.

to fibers on the vacuum side of our custom KF40 SQS® pigtalled feedthrough. The fibers on the atmosphere side are then coupled to the squeezed light source and HD setup, similar to the one detailed in the next chapter, with the addition of a fibered EOM for PDH locking (not shown on the figure), using the DC output of the HD for example. We show the optical layout of the experiment in Fig. I.28, where we can see the various components needed to generate, inject, lock and detect squeezed light from the fibered MATE cavity. Using non PM fibers, care must be taken to properly control and optimize the polarization state injected into the cavity, as to maximize the coupling to the fundamental cavity mode. This can be achieved using fiber polarization controllers.

Regarding the squeezed light degradation, few loss channels are to be considered. First, the mode matching to the filter cavity η_{cav} needs to be optimized. We estimate a realistic value to be around 90% (although it can reach up to 99% with careful alignment). Additionally, the fiber injection, MATE cavity mode match and collection efficiencies η_c needs to be considered. We can hope for an optimal overall coupling of about 90% too. Finally the detection efficiency η_{hom} which bundles the photodiode quantum efficiency, the visibility and propagation losses needs to be considered. Assuming high quality photodiodes (quantum efficiency $\sim 99\%$), a good visibility ($\sim 98\%$) and low propagation losses ($\sim 99\%$), we can expect an overall detection efficiency of about 95%. The total efficiency then reads $\eta_{\text{tot}} = \eta_{\text{cav}} \times \eta_c \times \eta_{\text{hom}} \sim 0.81$, which would lead to a degradation of about 1.15dB of squeezing for an initial level of 6dB injected into the cavity. This shows that achieving high overall efficiencies is crucial to observe significant squeezing levels at the output of the cavity. On

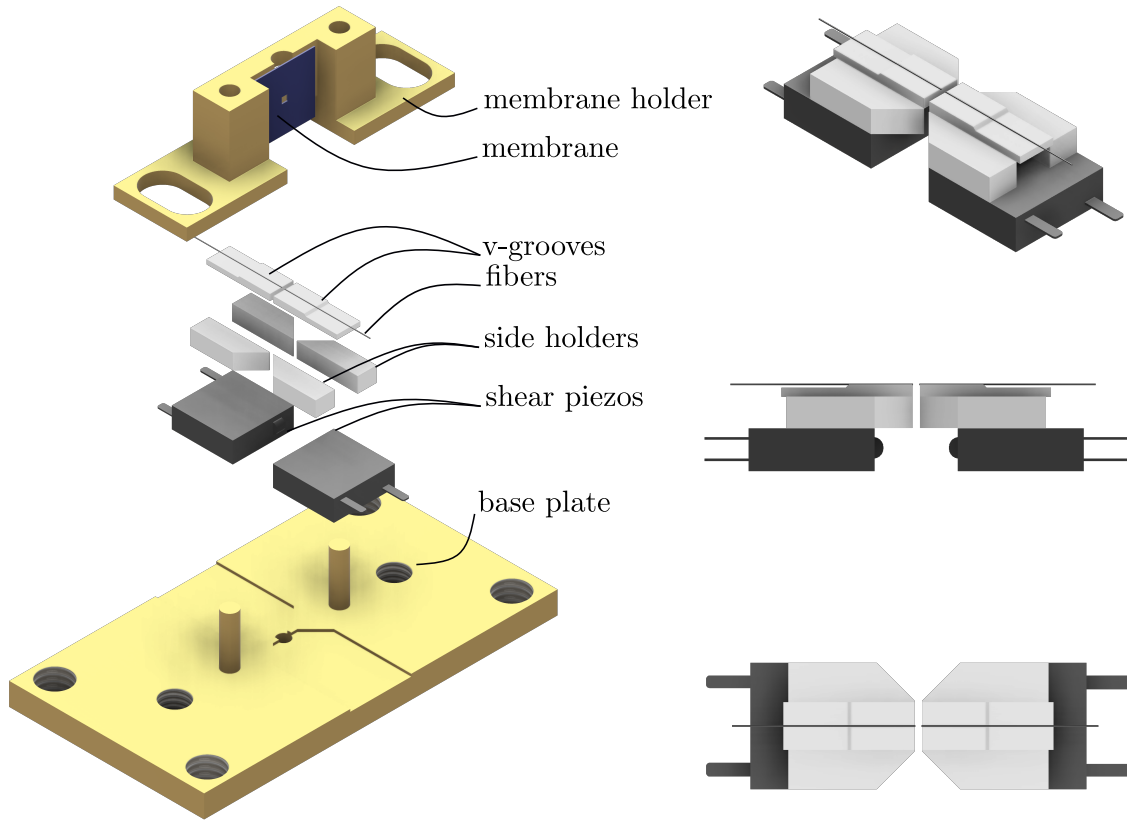


Fig. I.27 CAD model of the fibered MATE cavity assembly. (left) The membrane is glued/kapton taped to the membrane holder, which is then inserted and screwed to the cavity base plate. The fibered cavity is mounted on two piezo actuators used to tune the cavity length and the membrane position. (right) The fibers are held and glued in v-grooves positioned on the piezo actuators. Various views of the assembly are shown.

the other hand, pushing the initial squeezing level higher than 6dB would help rendering the experiment more resilient to losses.

I.4 Conclusion

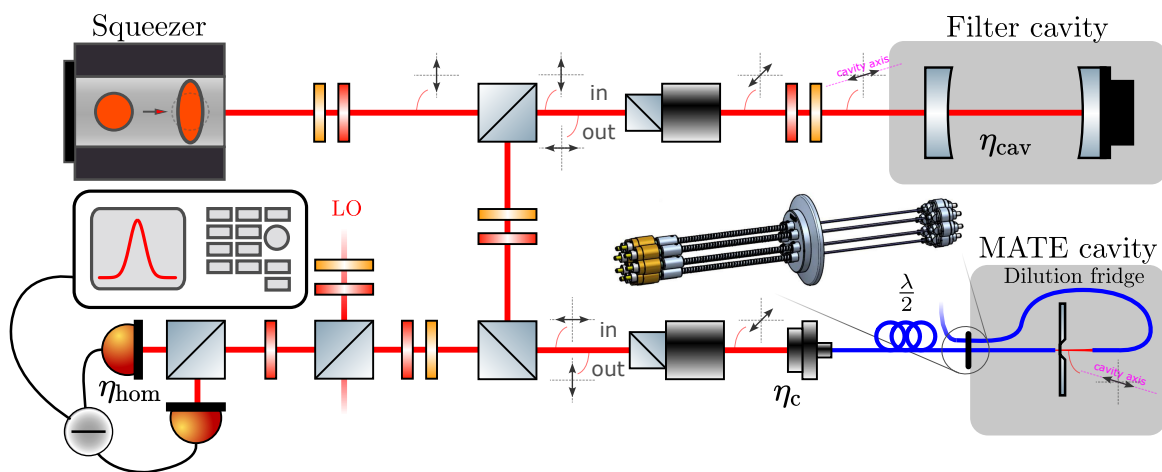


Fig. I.28 Prospective optical layout for the fibered MATE cavity experiment. The squeezed light source is similar to the one detailed in the next chapter. The frequency dependent bright squeezed field is injected into the MATE cavity using an LMA fiber, while the transmitted light is collected using a MM fiber. Not displayed here is a fibered EOM used to generate the PDH sidebands for locking the cavity. The PDH error signal would be obtained by demodulating the DC output of the HD, while the AC output would be used to monitor the mechanical spectrum.

Appendix A: Two-photon derivations

Field Quantization

From discrete to continuous modes

We consider the quantised electromagnetic field in a volume V along a single polarization direction. We assume the field to be a gaussian beam such that the quantization volume is written as $\mathcal{V} = \mathcal{A}L$, with \mathcal{A} the effective mode cross-sectional area, normal to the propagation direction z . The electric field operator can be written as

$$\hat{\mathbf{E}}(\mathbf{r}, t) = i \sum_{\ell} \sqrt{\frac{\hbar\omega_{\ell}}{2\varepsilon_0\mathcal{V}}} \left[\hat{a}_{\omega_{\ell}} \mathbf{f}_{\ell}(\mathbf{r}) e^{-i\omega_{\ell}t} - \hat{a}_{\omega_{\ell}}^{\dagger} \mathbf{f}_{\ell}^*(\mathbf{r}) e^{+i\omega_{\ell}t} \right], \quad (\text{I.8})$$

The index ℓ then labels the different modes, discrete at this point. The bosonic operators satisfy the canonical commutation relations

$$[\hat{a}_{\omega_{\ell}}, \hat{a}_{\omega_{\ell'}}^{\dagger}] = \delta_{\ell\ell'}, \quad [\hat{a}_{\omega_{\ell}}, \hat{a}_{\omega_{\ell'}}] = [\hat{a}_{\omega_{\ell}}^{\dagger}, \hat{a}_{\omega_{\ell'}}^{\dagger}] = 0.$$

We consider a the polarization along the $\hat{\mathbf{x}}$ direction where the hat denotes the unit vector and not an operator. The mode function can then be written as $\mathbf{f}_{\ell}(\mathbf{r}) = f_{\ell}(\mathbf{r})\hat{\mathbf{x}}$. We consider 1D wavevectors along the $+z$ direction i.e. positive k_{ℓ} only, such that in the limit of quantization volumes tending to infinity i.e. $L \rightarrow \infty$, the discrete sum over k modes turns into an integral over frequencies

$$\sum_{\ell}(\dots) \rightarrow \frac{L}{2\pi} \int_0^{\infty} dk(\dots) = \frac{1}{\Delta f} \int_0^{\infty} \frac{d\omega}{2\pi}(\dots) \quad \text{with} \quad \Delta f = \frac{c}{L}$$

using the dispersion relation $\omega = c|k|$. We then simply relabel $\hat{a}_{\omega_\ell} \rightarrow \hat{a}_\omega$, $f_\ell(\mathbf{r}) \rightarrow f(\mathbf{r}, \omega)$ and plug back into the original expression to have

$$\hat{\mathbf{E}}(\mathbf{r}, t) = i \int_0^\infty \frac{d\omega}{2\pi} \sqrt{\frac{\hbar\omega}{2\varepsilon_0\mathcal{A}c}} \left[\lim_{L \rightarrow \infty} \frac{\hat{a}[\Omega]}{\sqrt{\Delta f}} f(\mathbf{r}, \omega) e^{-i\omega t} - \lim_{L \rightarrow \infty} \frac{\hat{a}^\dagger[\Omega]}{\sqrt{\Delta f}} f^*(\mathbf{r}, \omega) e^{+i\omega t} \right] \hat{\mathbf{x}}.$$

and we can define the continuous bosonic operators as

$$\hat{a}[\omega] = \lim_{L \rightarrow \infty} \frac{\hat{a}_\omega}{\sqrt{\Delta f}} \quad \text{and} \quad \hat{a}^\dagger[\omega] = \lim_{L \rightarrow \infty} \frac{\hat{a}_\omega^\dagger}{\sqrt{\Delta f}}$$

such that the electric field operator reads

$$\hat{\mathbf{E}}(\mathbf{r}, t) = i \int_0^\infty \frac{d\omega}{2\pi} \mathcal{E} \left[\hat{a}[\omega] f(\mathbf{r}, \omega) e^{-i\omega t} - \hat{a}^\dagger[\omega] f^*(\mathbf{r}, \omega) e^{+i\omega t} \right] \hat{\mathbf{x}}, \quad \text{with} \quad \mathcal{E} = \sqrt{\frac{\hbar\omega}{2\varepsilon_0\mathcal{A}c}}.$$

Commutation relations

Using standard complex analysis techniques, the kronecker delta can be expressed as

$$\delta_{\ell\ell'} = \int_{-\pi}^{+\pi} dt \frac{e^{i(\ell-\ell')t}}{2\pi}.$$

Upon the aforementioned assumptions, we can introduce the frequency spacing $\Delta\omega = 2\pi\Delta f$ such that the discrete angular frequencies are written as $\omega_\ell = \ell\Delta\omega$. It then follows that $\ell - \ell' = (\omega_\ell - \omega_{\ell'})/\Delta\omega$. By changing the variable of integration from t to $t' = t/\Delta\omega$, we can rewrite the kronecker delta as

$$\delta_{\ell\ell'} = \int_{-L/2c}^{+L/2c} dt' \Delta f e^{i(\omega_\ell - \omega_{\ell'})t'}.$$

We can then see that in the limit of $L \rightarrow \infty$ i.e. $\Delta\omega \rightarrow 0$, the integral limits tend to infinity and the kronecker delta turns into a dirac delta such that

$$\lim_{L \rightarrow \infty} \frac{\delta_{\ell\ell'}}{\Delta f} = \int_{-\infty}^{+\infty} dt' e^{i(\omega - \omega')t'} = 2\pi\delta(\omega - \omega').$$

where we relabeled $\omega_\ell \rightarrow \omega$ and $\omega_{\ell'} \rightarrow \omega'$. The commutation relations for the continuous bosonic operators then read which satisfy the commutation relations

$$[\hat{a}[\omega], \hat{a}^\dagger[\omega']] = \lim_{L \rightarrow \infty} \frac{[\hat{a}_{\omega_\ell}, \hat{a}_{\omega_{\ell'}}^\dagger]}{\Delta f} = 2\pi\delta(\omega - \omega'), \quad [\hat{a}[\omega], \hat{a}[\omega']] = [\hat{a}^\dagger[\omega], \hat{a}^\dagger[\omega']] = 0.$$

Two photon formalism

Quadratures

We will now consider mode field frequencies $\omega = \omega_0 + \Omega$ around a carrier frequency ω_0 , such that the integral term becomes

$$\int_0^\infty \frac{d\omega}{2\pi}(\dots) \rightarrow \int_{-\omega_0}^\infty \frac{d\Omega}{2\pi}(\dots) \sim \int_{-B}^B \frac{d\Omega}{2\pi}(\dots) \sim \int_{-\infty}^\infty \frac{d\Omega}{2\pi}(\dots)$$

where B is the detection bandwidth, which is always much smaller than the optical frequency ω_0 . We can then safely extend the integral limits to infinity. Assuming that the mode function $f(\mathbf{r}, \omega)$ does not vary significantly over the bandwidth B , we can approximate it by its value at the carrier frequency $f(\mathbf{r}, \omega_0) \equiv f(\mathbf{r})$. Pulling out this term from the integral, one can then project the electric field operator onto both the proper polarization axis and this mode function such that the electric field operator becomes spatially independent and reads

$$\hat{E}(t) = i\mathcal{E}_0 \int_0^\infty \frac{d\Omega}{2\pi} \left[\hat{a}_+ e^{-i(\omega_0+\Omega)t} - \hat{a}_+^\dagger e^{+i(\omega_0+\Omega)t} + \hat{a}_- e^{-i(\omega_0-\Omega)t} - \hat{a}_-^\dagger e^{+i(\omega_0-\Omega)t} \right] \quad (\text{I.9})$$

with $\mathcal{E}_0 = \sqrt{\hbar\omega/2\varepsilon_0\mathcal{A}c}$, and where we additionally split the integral term in two, introducing negative and positive sideband frequencies whose annihilation and creation operators are written as

$$\hat{a}_\pm \equiv c_\pm \hat{a}[\omega_0 \pm \Omega] \quad \text{and} \quad \hat{a}_\pm^\dagger \equiv c_\pm \hat{a}^\dagger[\omega_0 \pm \Omega] \quad \text{with} \quad c_\pm = \sqrt{\frac{\omega_0 \pm \Omega}{\omega_0}}.$$

The commutators then read

$$[\hat{a}_\pm, \hat{a}_\pm^\dagger] = 2\pi c_\pm^2 \delta(\Omega - \Omega'), \quad [\hat{a}_\pm, \hat{a}_\mp] = [\hat{a}_\pm^\dagger, \hat{a}_\mp^\dagger] = 0$$

$$[\hat{a}_\pm, \hat{a}_\mp^\dagger] = 2\pi c_+ c_- \delta(\Omega + \Omega'), \quad [\hat{a}_\pm, \hat{a}_\mp] = [\hat{a}_\pm^\dagger, \hat{a}_\mp^\dagger] = 0$$

Computing expectation values for these operators in vacuum yields $\langle \hat{a}_\pm \rangle = \langle \hat{a}_\pm^\dagger \rangle = \langle 0 | \hat{a}_\pm^\dagger \hat{a}_\pm | 0 \rangle = 0$ and $\langle 0 | \hat{a}_\pm \hat{a}_\pm^\dagger | 0 \rangle = 2\pi c_\pm^2 \delta(0)$, which is consistent with the fact that no photons are present in these modes. We then regroup the terms along common quadratures $\cos \omega_0 t$ and $\sin \omega_0 t$ such that we get

$$\begin{aligned} \hat{E}(t) = i\mathcal{E}_0 & \left[\cos \omega_0 t \int_0^\infty \frac{d\Omega}{2\pi} \left[(\hat{a}_+ - \hat{a}_-^\dagger) e^{-i\Omega t} + (\hat{a}_- - \hat{a}_+^\dagger) e^{+i\Omega t} \right] \right. \\ & \left. - i \sin \omega_0 t \int_0^\infty \frac{d\Omega}{2\pi} \left[(\hat{a}_+ + \hat{a}_-^\dagger) e^{-i\Omega t} + (\hat{a}_- + \hat{a}_+^\dagger) e^{+i\Omega t} \right] \right] \end{aligned}$$

We now define the two-photon quadrature operators as

$$\hat{p}[\Omega] = \hat{a}_+ + \hat{a}_-^\dagger, \quad \hat{q}[\Omega] = i(\hat{a}_-^\dagger - \hat{a}_+)$$

such that the electric field operator reads

$$\begin{aligned} \hat{E}(t) &= \mathcal{E}_0 \left[\cos\left(\omega_0 t - \frac{\pi}{2}\right) \int_0^\infty \frac{d\Omega}{2\pi} [\hat{p}[\Omega] e^{-i\Omega t} + \hat{p}^\dagger[\Omega] e^{+i\Omega t}] \right. \\ &\quad \left. + \sin\left(\omega_0 t - \frac{\pi}{2}\right) \int_0^\infty \frac{d\Omega}{2\pi} [\hat{q}[\Omega] e^{-i\Omega t} + \hat{q}^\dagger[\Omega] e^{+i\Omega t}] \right] \end{aligned} \quad (\text{I.10})$$

where we used the fact that $\hat{p}^\dagger[\Omega] = \hat{p}[-\Omega]$ and $\hat{q}^\dagger[\Omega] = \hat{q}[-\Omega]$. The $\pi/2$ phase shifts originate from the leading factor i in the electric-field operator. Had the field operator been written without that prefactor (and without the minus sign in the creation-term), the resulting cosine and sine components would contain no such phase offset. The commutation relations for these quadrature operators read

$$\begin{aligned} [\hat{p}[\Omega], \hat{q}^\dagger[\Omega']] &= [\hat{q}[\Omega], \hat{p}^\dagger[\Omega']] = 4\pi i \delta(\Omega - \Omega') \\ [\hat{p}[\Omega], \hat{p}^\dagger[\Omega']] &= [\hat{q}[\Omega], \hat{q}^\dagger[\Omega']] = 4\pi \frac{\Omega}{\omega_0} \delta(\Omega - \Omega') \sim 0 \quad \text{if } \Omega \ll \omega_0 \\ [\hat{p}[\Omega], \hat{q}[\Omega']] &= [\hat{p}^\dagger[\Omega], \hat{q}^\dagger[\Omega']] = 0. \end{aligned}$$

In the limit where the sideband frequencies are small compared to the carrier frequency i.e. $\Omega \ll \omega_0$, we can approximate these prefactors by $c_\pm \sim 1$.

Expectations values in vacuum

We now proceed to evaluate the first and second momenta of our field operators in the vacuum state $|0\rangle$. As expected, the annihilation and creation operators have zero mean in vacuum, such that

$$\langle 0 | \hat{a}_+ | 0 \rangle = \langle 0 | \hat{a}_-^\dagger | 0 \rangle = 0$$

so it follows that

$$\langle 0 | \hat{p}[\Omega] | 0 \rangle = \langle 0 | \hat{q}[\Omega] | 0 \rangle = 0.$$

Building the two-photon quadrature column vector as

$$\hat{\mathbf{u}}[\Omega] = \begin{pmatrix} \hat{p}[\Omega] \\ \hat{q}[\Omega] \end{pmatrix}, \quad \text{we have} \quad \langle \hat{\mathbf{u}}[\Omega] \rangle = \begin{pmatrix} 0 \\ 0 \end{pmatrix}$$

where we see that, for a vacuum state, the full operator $\hat{\mathbf{u}}[\Omega]$ actually equates the fluctuating part $\delta\hat{\mathbf{u}}[\Omega] = \hat{\mathbf{u}}[\Omega] - \langle \hat{\mathbf{u}}[\Omega] \rangle$ since the mean value is zero. In the following, we will assume

that expectation values are always computed in the vacuum state unless otherwise specified (we will omit the $|0\rangle$ notation for clarity). We only wrote the results for the \hat{a}_+ and \hat{a}_-^\dagger operators as there are the ones composing the \hat{p} and \hat{q} quadratures, but the same results hold for the other sideband operators as well. We can then compute the second momenta of the annihilation and creation operators, yielding

$$\langle 0 | \hat{a}_-^\dagger \hat{a}_- | 0 \rangle = \langle 0 | \hat{a}_+ \hat{a}_- | 0 \rangle = \langle 0 | \hat{a}_-^\dagger \hat{a}_+^\dagger | 0 \rangle = 0$$

$$\langle 0 | \hat{a}_\pm \hat{a}_\pm^\dagger | 0 \rangle = 2\pi\delta(\Omega - \Omega') .$$

Using these relations, we can compute the second momenta for the two-photon quadrature operators as

$$\begin{aligned} \langle 0 | \hat{p}[\Omega] \hat{p}^\dagger[\Omega'] | 0 \rangle &= \langle 0 | \hat{a}_+ \hat{a}_+^\dagger + \hat{a}_+ \hat{a}_- + \hat{a}_-^\dagger \hat{a}_+^\dagger + \hat{a}_-^\dagger \hat{a}_- | 0 \rangle \\ &= 2\pi\delta(\Omega - \Omega') , \\ \langle 0 | \hat{q}[\Omega] \hat{q}^\dagger[\Omega'] | 0 \rangle &= 2\pi\delta(\Omega - \Omega') . \end{aligned}$$

as well as

$$\langle 0 | \hat{p}[\Omega] \hat{q}^\dagger[\Omega'] | 0 \rangle = -\langle 0 | \hat{q}^\dagger[\Omega] \hat{p}[\Omega'] | 0 \rangle = i2\pi\delta(\Omega - \Omega') .$$

Using the expression for the symmetrized double sided covariance matrix given in the main text, we can compute the covariance matrix for the two-photon quadrature operators in vacuum as

$$\begin{aligned} \mathbf{S}[\Omega] &= \frac{1}{2} \int \frac{\delta\Omega'}{2\pi} \langle \{ \delta\hat{\mathbf{u}}[\Omega], \delta\hat{\mathbf{u}}^\dagger[\Omega'] \} \rangle \\ &= \frac{1}{2} \int \frac{\delta\Omega'}{2\pi} \begin{pmatrix} \langle \{\hat{p}[\Omega], \hat{p}^\dagger[\Omega']\} \rangle & \langle \{\hat{p}[\Omega], \hat{q}^\dagger[\Omega']\} \rangle \\ \langle \{\hat{q}[\Omega], \hat{p}^\dagger[\Omega']\} \rangle & \langle \{\hat{q}[\Omega], \hat{q}^\dagger[\Omega']\} \rangle \end{pmatrix} \\ &= \frac{1}{2} \int \frac{\delta\Omega'}{2\pi} \begin{pmatrix} 2 \cdot 2\pi\delta(\Omega - \Omega') & 0 \\ 0 & 2 \cdot 2\pi\delta(\Omega - \Omega') \end{pmatrix} \\ &= \begin{pmatrix} 1 & 0 \\ 0 & 1 \end{pmatrix} = \mathbf{1} . \end{aligned}$$

The vacuum state then features vacuum fluctuations of unity in both quadratures, across all sideband frequencies Ω , and no correlations between the quadratures.

States and Operators in the Two-Photon Formalism

In a similar fashion as in the single-mode case, we can define the displacement operator as

$$\hat{D}(\alpha) = \exp \left(\int_{-\infty}^{\infty} \frac{d\Omega}{2\pi} [\alpha(\Omega) \hat{a}_-^\dagger - \alpha^*(\Omega) \hat{a}_+] \right)$$

as well as a squeezing operator

$$\hat{S}(r, \theta) = \exp \left(r \int_{-\infty}^{\infty} \frac{d\Omega}{2\pi} [e^{-i2\theta(\Omega)} \hat{a}_+ \hat{a}_- - e^{i2\theta(\Omega)} \hat{a}_+^\dagger \hat{a}_-^\dagger] \right)$$

where r is the squeezing factor and $\theta(\Omega)$ the squeezing angle. Here we assumed the squeezing parameter to be frequency independent, but one can easily generalize to a frequency dependent squeezing parameter $r(\Omega)$. Using the sidebands annihilation operators defined previously, we can compute the action of the displacement and squeezing operators on the annihilation operator as

$$\begin{aligned} \hat{D}^\dagger(\alpha) \hat{a}_+ \hat{D}(\alpha) &= \hat{a}_+ + \alpha(\Omega), \\ \hat{S}^\dagger(r, \theta) \hat{a}_+ \hat{S}(r, \theta) &= \hat{a}_+ \cosh r - e^{i2\theta(\Omega)} \hat{a}_-^\dagger \sinh r. \end{aligned}$$

We consider a intial vacuum state $|0\rangle$, and we displace it by a coherent amplitude $\alpha(\Omega) = \alpha\delta(\Omega)$ i.e. a carrier, monochromatic field of complex amplitude α sitting at frequency 0 (we are in the frame rotating at ω_0 already since we factored out the $e^{-i\omega_0 t}$ term). The displacement operator then acts on the two photon quadrature operators as

$$\begin{aligned} \hat{D}^\dagger(\alpha) \hat{p}[\Omega] \hat{D}(\alpha) &= \hat{p}[\Omega] + 2 \operatorname{Re}\{\alpha\} \delta(\Omega), \\ \hat{D}^\dagger(\alpha) \hat{q}[\Omega] \hat{D}(\alpha) &= \hat{q}[\Omega] + 2 \operatorname{Im}\{\alpha\} \delta(\Omega). \end{aligned}$$

or in matrix form

$$\hat{D}^\dagger(\alpha) \hat{\mathbf{u}}[\Omega] \hat{D}(\alpha) = \hat{\mathbf{u}}[\Omega] + 2 \begin{pmatrix} \operatorname{Re}\{\alpha\} \\ \operatorname{Im}\{\alpha\} \end{pmatrix} \delta(\Omega).$$

In a similar fashion, the squeezing operator acts as

$$\begin{aligned} \hat{S}^\dagger(r, \theta) \hat{p}[\Omega] \hat{S}(r, \theta) &= \hat{p}[\Omega] (\cosh r - \sinh r \cos 2\theta) - \hat{q}[\Omega] \sin 2\theta \sinh r, \\ \hat{S}^\dagger(r, \theta) \hat{q}[\Omega] \hat{S}(r, \theta) &= \hat{q}[\Omega] (\cosh r + \sinh r \cos 2\theta) - \hat{p}[\Omega] \sin 2\theta \sinh r. \end{aligned}$$

and its matrix form reads

$$\hat{S}^\dagger(r, \theta) \hat{\mathbf{u}}[\Omega] \hat{S}(r, \theta) = \mathbf{S}(r, \theta) \hat{\mathbf{u}}[\Omega], \quad \text{with} \quad \mathbf{S}(r, \theta) = \begin{pmatrix} \cosh r - \sinh r \cos 2\theta & -\sin 2\theta \sinh r \\ -\sin 2\theta \sinh r & \cosh r + \sinh r \cos 2\theta \end{pmatrix}.$$

The state resulting from applying both operators onto the vacuum is written as

$$|\psi\rangle = \hat{S}(r, \theta) \hat{D}(\alpha) |0\rangle$$

and describes a squeezed coherent state, or bright squeezed state. One can then set the coherent amplitude to 0 as to get a vacuum squeezed state, or set the squeezing parameter to 0 to get a coherent state. This is one of the most generic gaussian state one can define in quantum optics. We write the operator product as $\hat{D}\hat{S}$ and we drop the Ω dependencies to lighten the notation, such that applying them to the field operators yields

$$\begin{aligned} \hat{D}^\dagger \hat{S}^\dagger \hat{a}_+ \hat{S} \hat{D} &= \hat{a}_+ \cosh r - e^{i2\theta} \hat{a}_-^\dagger \sinh r + \gamma \delta(\Omega) \\ \hat{D}^\dagger \hat{S}^\dagger \hat{a}_-^\dagger \hat{S} \hat{D} &= \hat{a}_-^\dagger \cosh r - e^{-i2\theta} \hat{a}_+ \sinh r + \gamma^* \delta(\Omega). \end{aligned}$$

as well as the quadratures

$$\begin{aligned} \hat{D}^\dagger \hat{S}^\dagger \hat{p} \hat{S} \hat{D} &= \hat{p}(\cosh r - \cos 2\theta \sinh r) - \hat{q} \sin 2\theta \sinh r + 2 \operatorname{Re}\{\gamma\} \delta(\Omega), \\ \hat{D}^\dagger \hat{S}^\dagger \hat{q} \hat{S} \hat{D} &= \hat{q}(\cosh r + \cos 2\theta \sinh r) - \hat{p} \sin 2\theta \sinh r + 2 \operatorname{Im}\{\gamma\} \delta(\Omega). \end{aligned}$$

where we introduced the scalar part of these transformed operators as

$$\begin{aligned} \gamma &= \alpha \cosh r - \alpha^* e^{i2\theta} \sinh r, \\ \gamma^* &= \alpha^* \cosh r - \alpha e^{-i2\theta} \sinh r. \end{aligned}$$

The matrix form then reads

$$\hat{D}^\dagger \hat{S}^\dagger \hat{\mathbf{u}} \hat{S} \hat{D} = \mathbf{S}(r, \theta) \hat{\mathbf{u}} + 2 \begin{pmatrix} \operatorname{Re}\{\gamma\} \\ \operatorname{Im}\{\gamma\} \end{pmatrix} \delta(\Omega).$$

The mean values is then straightforward to compute

$$\begin{aligned} \langle \hat{D}^\dagger \hat{S}^\dagger \hat{\mathbf{u}} \hat{S} \hat{D} \rangle &= \mathbf{S}(r, \theta) \langle \hat{\mathbf{u}} \rangle + 2 \begin{pmatrix} \operatorname{Re}\{\gamma\} \\ \operatorname{Im}\{\gamma\} \end{pmatrix} \delta(\Omega) \\ &= 2 \begin{pmatrix} \operatorname{Re}\{\gamma\} \\ \operatorname{Im}\{\gamma\} \end{pmatrix} \delta(\Omega). \end{aligned}$$

such that the fluctuating part reads

$$\delta \hat{\mathbf{u}} = \hat{D}^\dagger \hat{S}^\dagger \hat{\mathbf{u}} \hat{S} \hat{D} - \langle \hat{D}^\dagger \hat{S}^\dagger \hat{\mathbf{u}} \hat{S} \hat{D} \rangle = \mathbf{S}(r, \theta) \hat{\mathbf{u}} \quad \text{and} \quad \delta \hat{\mathbf{u}}^\dagger = \hat{\mathbf{u}}^\dagger \mathbf{S}(r, \theta).$$

where we used the fact that the squeezing matrix is symmetric, i.e. $\mathbf{S} = \mathbf{S}^T$. The covariance matrix for this squeezed coherent state then reads

$$\begin{aligned} \mathbf{S}[\Omega] &= \frac{1}{2} \int \frac{\delta\Omega'}{2\pi} \langle \{\delta \hat{\mathbf{u}}[\Omega], \delta \hat{\mathbf{u}}^\dagger[\Omega']\} \rangle \\ &= \frac{1}{2} \int \frac{\delta\Omega'}{2\pi} \langle \{\mathbf{S}(r, \theta) \hat{\mathbf{u}}[\Omega], \hat{\mathbf{u}}^\dagger[\Omega'] \mathbf{S}(r, \theta)\} \rangle \\ &= \mathbf{S}(r, \theta) \left(\frac{1}{2} \int \frac{\delta\Omega'}{2\pi} \langle \{\hat{\mathbf{u}}[\Omega], \hat{\mathbf{u}}^\dagger[\Omega']\} \rangle \right) \mathbf{S}(r, \theta) \\ &= \mathbf{S}(r, \theta) \cdot \mathbf{1} \cdot \mathbf{S}(r, \theta) = \mathbf{S}(r, \theta)^2 \\ &= \begin{pmatrix} \cosh 2r - \sinh 2r \cos 2\theta & -\sin 2\theta \sinh 2r \\ -\sin 2\theta \sinh 2r & \cosh 2r + \sinh 2r \cos 2\theta \end{pmatrix}. \end{aligned}$$

such that the expectation values are computed as

$$\begin{aligned} \langle \hat{a}_+ \rangle &= \gamma \delta(\Omega) \\ \langle \hat{a}_-^\dagger \rangle &= \gamma^* \delta(\Omega) \\ \langle \hat{p} \rangle &= 2 \operatorname{Re}\{\gamma\} \delta(\Omega) \\ \langle \hat{q} \rangle &= 2 \operatorname{Im}\{\gamma\} \delta(\Omega). \end{aligned}$$

and we compute the expectation value of our two-photon annihilation operator as

$$\langle \hat{a}_+ \rangle = \alpha \delta(\Omega) \quad \text{and} \quad \langle \hat{a}_-^\dagger \rangle = \alpha^* \delta(\Omega)$$

as well as their second momenta as

The electric field operator finally reads

$$\hat{\mathbf{E}}(\mathbf{r}, t) = i \sqrt{\frac{\hbar\omega_0}{\varepsilon_0 \mathcal{A}c}} \left[\int_{-\infty}^{\infty} \frac{d\Omega}{2\pi} \left[\hat{a}_\Omega e^{-i(\omega_0 + \Omega)t} - \hat{a}_\Omega^\dagger e^{+i(\omega_0 + \Omega)t} \right] \right] \quad (\text{I.11})$$

such that the classical part of the electric field reads

We start from the standard single-mode field quantization in terms of annihilation and

creation operators \hat{a} and \hat{a}^\dagger :

$$\hat{E}(t) = \sqrt{\frac{\hbar\omega_0}{2\varepsilon_0}} (\hat{a}e^{-i\omega_0 t} + \hat{a}^\dagger e^{i\omega_0 t}).$$

and we now make our bosonic operators time-dependent, $\hat{a} \rightarrow \hat{a}(t)$, to account for sidebands around the carrier frequency ω_0 . Using the Fourier transform convention

$$\hat{a}(t) = \int_{-\infty}^{+\infty} \frac{d\Omega}{2\pi} \hat{a}[\Omega] e^{-i\Omega t},$$

we rewrite the field operator as

$$\hat{E}(t) = \sqrt{\frac{\hbar\omega_0}{2\varepsilon_0}} \int_{-\infty}^{+\infty} \frac{d\Omega}{2\pi} (\hat{a}[\Omega] e^{-i(\omega_0+\Omega)t} + \hat{a}^\dagger[\Omega] e^{i(\omega_0+\Omega)t}).$$

$$\hat{p}[\Omega] = 2|\alpha|(\delta[\Omega] + \text{Re}\{\varepsilon[\Omega]\}) + \delta\hat{p}[\Omega], \quad (\text{I.12})$$

$$\hat{p}[\Omega] \hat{p}[\Omega'] = 4|\alpha|^2 (\delta[\Omega]S[\Omega'] + \delta[\Omega]\text{Re}\{\varepsilon[\Omega']\} + \delta[\Omega']\text{Re}\{\varepsilon[\Omega]\} + \text{Re}\{\varepsilon[\Omega]\}\text{Re}\{\varepsilon[\Omega']\}) + \delta\hat{p}[\Omega] \delta\hat{p}[\Omega'], \quad (\text{I.13})$$

$$\langle \dots \rangle = 4|\alpha|^2 (\delta(\Omega)\delta(\Omega') + \frac{\varepsilon}{2}\delta(\Omega)\delta(\Omega' - \Omega_m) + \frac{\varepsilon}{2}\delta(\Omega)\delta(\Omega' + \Omega_m)) \quad (\text{I.14})$$

$$+ \frac{\varepsilon}{2}\delta(\Omega')\delta(\Omega - \Omega_m) + \frac{\varepsilon}{2}\delta(\Omega')\delta(\Omega + \Omega_m) \quad (\text{I.15})$$

$$+ \frac{\varepsilon^2}{4} [\delta(\Omega - \Omega_m)\delta(\Omega' + \Omega_m) + \delta(\Omega - \Omega_m)\delta(\Omega' - \Omega_m) \quad (\text{I.16})$$

$$+ \delta(\Omega + \Omega_m)\delta(\Omega' + \Omega_m) + \delta(\Omega + \Omega_m)\delta(\Omega' - \Omega_m)] \big) + \langle \delta p[\Omega] \delta p[\Omega'] \rangle. \quad (\text{I.17})$$

Derivation of the optimal angle

Optimal fixed homodyne angle with complex \mathcal{K}

Assume the measured (reflected) quadrature is

$$\delta q_r = \delta q_{\text{in}} + \mathcal{K} \delta p_{\text{in}},$$

so that, for any input covariance matrix S^{in} ,

$$S_{qq}^r = S_{qq}^{\text{in}} + |\mathcal{K}|^2 S_{pp}^{\text{in}} + 2 \text{Re}\{\mathcal{K}\} S_{pq}^{\text{in}}.$$

For an input squeezed state of strength R and angle θ ,

$$S^{\text{in}}(r, \theta) = \begin{pmatrix} \cosh 2r + \sinh 2r \cos 2\theta & -\sinh 2r \sin 2\theta \\ -\sinh 2r \sin 2\theta & \cosh 2r - \sinh 2r \cos 2\theta \end{pmatrix}.$$

Hence

$$\begin{aligned} S_{qq}^r(\theta) &= \cosh 2r - \sinh 2r \cos 2\theta + |\mathcal{K}|^2(\cosh 2r + \sinh 2r \cos 2\theta) - 2 \operatorname{Re}\{\mathcal{K}\} \sinh 2r \sin 2\theta \\ &= (1 + |\mathcal{K}|^2) \cosh 2r - (1 - |\mathcal{K}|^2) \sinh 2r \cos 2\theta - 2 \operatorname{Re}\{\mathcal{K}\} \sinh 2r \sin 2\theta. \end{aligned} \quad (\text{I.18})$$

Optimal fixed angle. Differentiate (I.18) w.r.t. θ and set to zero:

$$\frac{\partial S_{qq}^r}{\partial \theta} = 2 \sinh 2r \left[(1 - |\mathcal{K}|^2) \sin 2\theta - 2 \operatorname{Re}\{\mathcal{K}\} \cos 2\theta \right] = 0,$$

which gives the optimal fixed readout angle

$$\tan(2\theta_{\text{opt}}) = \frac{2 \operatorname{Re}\{\mathcal{K}\}}{1 - |\mathcal{K}|^2} \quad (\text{I.19})$$

Writing $\mathcal{K} = |\mathcal{K}|e^{i\varphi_m}$ one may also use

$$\tan(2\theta_{\text{opt}}) = \frac{2|\mathcal{K}| \cos \varphi_m}{1 - |\mathcal{K}|^2}.$$

Minimum attained value. Plugging the optimal angle back into (I.18) then yields

$$S_{qq,\text{min}}^r = (1 + |\mathcal{K}|^2) \cosh 2r - \sqrt{(1 - |\mathcal{K}|^2)^2 + (2 \operatorname{Re}\{\mathcal{K}\})^2} \sinh 2r, \quad (\text{I.20})$$

Lower bound and the real- \mathcal{K} case. In the free mass limit, \mathcal{K} is purely real, so that $\varphi_m = 0$ and $\operatorname{Re}\{\mathcal{K}\} = |\mathcal{K}|$. In this case, the minimum variance (I.20) reduces to

$$S_{qq,\text{min}}^r = (1 + |\mathcal{K}|^2)e^{-2r}$$

resultst to be used

$$\frac{d\mathcal{K}}{d\Omega}(\Omega) = \frac{C^2}{2} \hbar \frac{2\Omega + i\gamma_m}{m (\Omega_m^2 - \Omega^2 - i\gamma_m\Omega)^2}. \quad (\text{I.21})$$

$$\left. \frac{d\mathcal{K}}{d\Omega} \right|_{\Omega=\Omega_m} = -\frac{C^2 \hbar}{2m} \frac{2\Omega_m + i\gamma_m}{\gamma_m^2 \Omega_m^2} = -\frac{C^2 \hbar}{2m} \left(\frac{2}{\gamma_m^2 \Omega_m} + i \frac{1}{\gamma_m \Omega_m^2} \right). \quad (\text{I.22})$$

Appendix B: Error Signals

In this appendix, we detail calculation details not mentionned in the main text regarding the detection of optical fields and error signals.

Direct detection error signals

We describe the completely generic photocurrent obtained from direct detection of two optical fields interfering on a photodetector. We consider two fields with field operators \hat{a} and \hat{a}' , with classical amplitudes $|\bar{\alpha}|$ and $|\bar{\alpha}'|e^{-i(\Delta\omega t+\phi)}$ as well as fluctuations $\delta\hat{a}$ and $\delta\hat{a}'e^{-i(\Delta\omega t+\phi)}$ i.e. $\bar{\alpha}$ is real. The photocurrent operator is then given by

$$\hat{I} = \left(|\bar{\alpha}| + \delta\hat{a}^\dagger + |\bar{\alpha}'|e^{i(\Delta\omega t+\phi)} + \delta\hat{a}'^\dagger e^{i(\Delta\omega t+\phi)} \right) \left(|\bar{\alpha}| + \delta\hat{a} + |\bar{\alpha}'|e^{-i(\Delta\omega t+\phi)} + \delta\hat{a}' e^{-i(\Delta\omega t+\phi)} \right)$$

We remind here the expression for the amplitude and phase quadratures for both fields

$$\delta\hat{p} = \delta\hat{a} + \delta\hat{a}^\dagger, \quad \delta\hat{q} = -i(\delta\hat{a} - \delta\hat{a}^\dagger),$$

and

$$\delta\hat{p}' = e^{-i(\Delta\omega t+\phi)}\delta\hat{a}' + e^{i(\Delta\omega t+\phi)}\delta\hat{a}'^\dagger, \quad \delta\hat{q}' = -i(e^{-i(\Delta\omega t+\phi)}\delta\hat{a}' - e^{i(\Delta\omega t+\phi)}\delta\hat{a}'^\dagger).$$

Expanding this expression and keeping only terms up to first order in the fluctuations, we find

$$\begin{aligned} \hat{I}(t) \approx & |\bar{\alpha}|^2 + |\bar{\alpha}'|^2 + 2|\bar{\alpha}||\bar{\alpha}'| \cos(\Delta\omega t + \phi) \\ & + |\bar{\alpha}|(\delta\hat{p} + \delta\hat{p}') \\ & + |\bar{\alpha}'| \cos(\Delta\omega t + \phi)(\delta\hat{p} + \delta\hat{p}') \\ & + |\bar{\alpha}'| \sin(\Delta\omega t + \phi)(\delta\hat{q} - \delta\hat{q}') \end{aligned}$$

The first line corresponds to the classical DC and beatnote terms, while the remaining lines correspond to the fluctuations. We will now explore the different detection regimes covered in the main text.

Single field detection

Let's first consider the single field case where we get rid of all terms related to \hat{a}' . The photocurrent operator then reduces to

$$\hat{I} \approx |\bar{\alpha}|^2 + |\bar{\alpha}|\delta\hat{p}.$$

The photocurrent fluctuations are then directly proportional to the amplitude quadrature fluctuations of the input field, scaled by the classical amplitude.

Two fields detection

Let's first consider two fields with the same frequency, i.e. $\Delta\omega = 0$. The photocurrent operator then reads

$$\begin{aligned}\hat{I} \approx & |\bar{\alpha}|^2 + |\bar{\alpha}'|^2 + 2|\bar{\alpha}||\bar{\alpha}'| \cos(\phi) \\ & + |\bar{\alpha}| (\delta\hat{p} + \delta\hat{p}') \\ & + |\bar{\alpha}'| \cos(\phi) (\delta\hat{p} + \delta\hat{p}') \\ & + |\bar{\alpha}'| \sin(\phi) (\delta\hat{q} - \delta\hat{q}')\end{aligned}$$

where the mean field is a simple interference between the two fields, while the fluctuations depend on both amplitude and phase quadratures of the two fields. By adjusting the relative phase ϕ , one can select which quadrature is measured. For example, setting $\phi = 0$ selects the amplitude quadratures, while setting $\phi = \pi/2$ selects the phase quadratures. The issue is that in this case, both fields contribute to the measured quadrature fluctuations, which is not desired when probing sub shotnoise fluctuations of a signal (the LO will add its own fluctuations).

Two fields detection with frequency offset

Now, we consider the case where the two fields have a frequency offset $\Delta\omega \neq 0$. The mean photocurrent then contains a beatnote at frequency $\Delta\omega$ and reads

$$\bar{I} = |\bar{\alpha}|^2 + |\bar{\alpha}'|^2 + 2|\bar{\alpha}||\bar{\alpha}'| \cos(\Delta\omega t + \phi).$$

such that demodulating the photocurrent at frequency $\Delta\omega' \sim \Delta\tilde{\omega}$ with phase $\tilde{\phi}$ and low-pass filtering yields

$$\bar{I}_{\text{demod}} \approx |\bar{\alpha}||\bar{\alpha}'| \cos((\Delta\omega - \Delta\tilde{\omega})t + \phi - \tilde{\phi}).$$

This very signal can then be used to lock the frequency of an auxiliary laser to the desired frequency offset $\Delta\tilde{\omega}$ from the main laser. However, this signal featuring many zero crossings, one needs to tune the auxiliary laser frequency close enough to the desired offset so that it

ensures the feedback loop locks to the correct zero crossing. This is generally done manually by scanning the auxiliary laser frequency until the right zero crossing is found, confirmed by monitoring the beatnote on a spectrum analyzer.

PDH error signal

the Pound-Drever-Hall (PDH) error signal starting from the real, quantum-normalized phase-modulated electric field expression. We aim to show how the demodulated signal is a linear combination of the real and imaginary parts of the cavity reflection coefficient, with the demodulation phase selecting the appropriate quadrature for locking.

Input Phase-Modulated Field

The electric field at the input of the cavity is assumed to be a coherent state that has been phase-modulated at frequency Ω , such that the classical (real) electric field takes the form:

$$E_{\text{cl}}^{(\text{PM})}(t) = i\sqrt{\frac{\hbar\omega_0}{2\varepsilon_0}} \alpha_0 \left[e^{-i\omega_0 t} - e^{i\omega_0 t} + \frac{i\epsilon_\phi}{2} (e^{-i(\omega_0-\Omega)t} + e^{i(\omega_0-\Omega)t}) + \frac{i\epsilon_\phi}{2} (e^{-i(\omega_0+\Omega)t} + e^{i(\omega_0+\Omega)t}) \right] \quad (\text{I.23})$$

where α_0 is the coherent amplitude of the carrier, $\epsilon_\phi \ll 1$ is a small modulation index (related to the phase modulation depth), and ω_0 is the optical carrier frequency. This field includes both the positive and negative frequency components, as expected for a physical (Hermitian) electric field operator.

Reflection from the Cavity

Each frequency component of the field is reflected with a complex frequency-dependent amplitude reflection coefficient $r(\omega)$, such that the reflected field is:

$$\begin{aligned} E_{\text{refl}}(t) = & i\sqrt{\frac{\hbar\omega_0}{2\varepsilon_0}} \alpha_0 \left[r(\omega_0)e^{-i\omega_0 t} - r^*(\omega_0)e^{i\omega_0 t} \right. \\ & + \frac{i\epsilon_\phi}{2} (r(\omega_0 - \Omega)e^{-i(\omega_0-\Omega)t} + r^*(\omega_0 - \Omega)e^{i(\omega_0-\Omega)t}) \\ & \left. + \frac{i\epsilon_\phi}{2} (r(\omega_0 + \Omega)e^{-i(\omega_0+\Omega)t} + r^*(\omega_0 + \Omega)e^{i(\omega_0+\Omega)t}) \right] \end{aligned} \quad (\text{I.24})$$

Photodetected Intensity

The photodetector measures the intensity:

$$I(t) \propto |E_{\text{refl}}(t)|^2$$

We isolate the terms oscillating at Ω , which arise from the interference between the carrier and sideband components. Keeping only the beat terms between the carrier and sidebands, we find:

$$I(t) \supset \epsilon_\phi \cdot \operatorname{Re}[A_+ - A_-] \cos(\Omega t) + \epsilon_\phi \cdot \operatorname{Im}[A_+ - A_-] \sin(\Omega t) \quad (\text{I.25})$$

where we define:

$$A_\pm = r(\omega_0)r^*(\omega_0 \pm \Omega)$$

Demodulation with Arbitrary Phase

The signal is demodulated using a local oscillator $\cos(\Omega t + \phi)$, where ϕ is the demodulation phase. Using trigonometric identities:

$$\cos(\Omega t + \phi) = \cos(\Omega t) \cos \phi - \sin(\Omega t) \sin \phi$$

we multiply Equation (I.25) and low-pass filter to obtain:

$$\epsilon_{\text{PDH}}(\phi) \propto \epsilon_\phi \{\operatorname{Re}[A_+ - A_-] \cos \phi + \operatorname{Im}[A_+ - A_-] \sin \phi\} \quad (\text{I.26})$$

Sidebands Far Off-Resonance Approximation

In the standard PDH regime, the modulation frequency is much greater than the cavity linewidth:

$$\Omega \gg \kappa$$

so the sidebands are far off-resonance. This means:

$$r(\omega_0 \pm \Omega) \approx 1 \Rightarrow A_\pm \approx r(\omega_0)$$

and therefore:

$$A_+ - A_- \approx 0$$

However, if we retain the asymmetry between the sidebands (e.g., due to dispersion), or keep the finite detuning contribution, we approximate:

$$A_+ - A_- \approx r(\omega_0) [r^*(\omega_0 + \Omega) - r^*(\omega_0 - \Omega)] = r(\omega_0) \Delta r^*$$

Final Result

Substituting into Equation (I.26), we obtain:

$$\epsilon_{\text{PDH}}(\phi) \propto \epsilon_\phi \{\operatorname{Re}[r(\omega_0) \Delta r^*] \cos \phi + \operatorname{Im}[r(\omega_0) \Delta r^*] \sin \phi\} \quad (\text{I.27})$$

In the limit where $\Delta r^* \rightarrow 1$ (normalized, symmetric sidebands), this simplifies to:

$$\epsilon_{\text{PDH}}(\omega_0, \phi) \propto \cos \phi \cdot \text{Re}[r(\omega_0)] + \sin \phi \cdot \text{Im}[r(\omega_0)] \quad (\text{I.28})$$

7. Interpretation

Equation (I.28) shows that the demodulated error signal is a linear superposition of the real and imaginary parts of the complex reflection coefficient. The demodulation phase ϕ selects the detected quadrature:

- $\phi = 0$: error signal is proportional to $\text{Re}[r]$ — symmetric around resonance, not suitable for locking.
- $\phi = \pi/2$: error signal is proportional to $\text{Im}[r]$ — antisymmetric, ideal dispersive error signal.
- $\phi \neq 0, \pi/2$: mixes quadratures, possibly introducing offset or distortion.

This derivation makes explicit how the PDH method uses phase-sensitive detection to extract the component of the reflection coefficient that varies linearly with detuning, enabling precise feedback locking of the laser to the cavity resonance.

Appendix C: Three Mirror cavities

In this appendix, we detail calculation details not mentionned in the main text regarding three-mirror cavities.

Three-mirror cavity fields

We consider an input coupler mirror with amplitude reflectivity and transmissivity r_1 and t_1 , a second mirror with r_m and t_m (to be consistent with the main text) and a third mirror with r_2 and t_2 . We will consider the input and output mirrors to be HR mirrors i.e. $R_i = |r_i|^2 \sim 1$ and $T_i = |t_i|^2 \ll 1$ for $i = 1, 2$. This will allow us to neglect terms in t_1^2 and t_2^2 in the following calculations. The input-output relation at various coupler interfaces read

$$\begin{aligned}\hat{a}_R &= t_m \hat{a}_L + r_m \hat{a}'_R \\ \hat{a}'_L &= t_m \hat{a}'_R + r_m \hat{a}_L\end{aligned}$$

as well as the reflections on the input and output couplers

$$\begin{aligned}\hat{a}_L &= -r_1 \hat{a}_R e^{i\phi_L} + t_1 \hat{a}_{\text{in}} \sim -\hat{a}_R e^{i\phi_L} + t_1 \hat{a}_{\text{in}} \\ \hat{a}'_R &= -r_2 \hat{a}_R e^{i\phi_R} \sim \hat{a}_R e^{i\phi_R}\end{aligned}$$

where $\phi_L = 2kL_1$ and $\phi_R = 2kL_2$ are the lengths of the two sub-cavities. Here we will consider the reflection coefficient of the input/output couplers to be $r_i \sim -1$ for $i = 1, 2$, and $r_m = |r_m|$ and $t_m = i|t_m|$ for the middle mirror / membrane. Injecting the second system in the first one yields

$$\begin{aligned}(1 - r_m e^{i\phi_R}) \hat{a}_R &= t_m e^{i\phi_L} \hat{a}'_L + t_m t_1 \hat{a}_{\text{in}} \\ (1 - r_m e^{i\phi_L}) \hat{a}'_L &= t_m e^{i\phi_R} \hat{a}_R + r_m t_1 \hat{a}_{\text{in}}\end{aligned}$$

such that isolating the \hat{a}_{in} and considering the mean fields yields

$$\frac{\alpha_R}{\alpha'_L} = \frac{|t_m|(2|r_m| \sin \phi_L + i)}{|r_m|^2 - e^{i\phi_R}}$$

and the power ration for a driven cavity yields

$$\frac{P_R}{P'_L} = \frac{|t_m|^2(4|r_m|^2 \sin^2 \phi_L + 1)}{|r_m|^4 - 2|r_m|^2 \cos \phi_R + 1}$$

Bibliography

- [1] Andreas Muller et al. “Ultrahigh-finesse, low-mode-volume Fabry–Perot microcavity”. In: *Opt. Lett.* 35.13 (July 2010), pp. 2293–2295 (cit. on p. 4).
- [2] D Hunger et al. “A fiber Fabry–Perot cavity with high finesse”. In: *New J. Phys.* 12.6 (June 2010), p. 065038 (cit. on p. 4).
- [3] Georg Enzian et al. “Phononically shielded photonic-crystal mirror membranes for cavity quantum optomechanics”. In: *Optics Express* 31.8 (Apr. 10, 2023). Publisher: Optica Publishing Group, pp. 13040–13052 (cit. on p. 4).
- [4] A H Ghadimi et al. “Elastic strain engineering for ultralow mechanical dissipation”. In: *Science* 360.6390 (May 2018), pp. 764–768 (cit. on p. 4).
- [5] J. D. Thompson et al. “Strong dispersive coupling of a high-finesse cavity to a micromechanical membrane”. In: *Nature* 452.7183 (2008), pp. 72–75 (cit. on pp. 5, 7).
- [6] A. M. Jayich et al. “Dispersive optomechanics: a membrane inside a cavity”. In: *New Journal of Physics* 10.9 (Sept. 2008), p. 095008 (cit. on p. 5).
- [7] Alex Amato. “Low Thermal Noise Coating for New Generation Gravitational-Wave Detectors”. Theses. Université de Lyon, Nov. 2019 (cit. on p. 5).
- [8] Alex Amato et al. “High-Reflection Coatings for Gravitational-Wave Detectors: State of The Art and Future Developments”. In: *Journal of Physics: Conference Series* 957.1 (Feb. 2018), p. 012006 (cit. on p. 5).
- [9] Himanshu Patange. “RF Transduction in a DC-Biased Superconducting Electromechanical System”. Theses. Sorbonne Université, Apr. 2025 (cit. on p. 6).
- [10] Norcada Inc. *High-Q Silicon Nitride Membranes*. <https://www.norcada.com/mems-products/high-q-silicon-nitride-membranes/>. Accessed: 2026-01-15. 2026 (cit. on p. 6).
- [11] RA Norte, JP Moura, and CA Regal. “Mechanical resonators for quantum optomechanics experiments at room temperature”. In: *Physical Review Letters* 116.14 (2016), p. 147202 (cit. on p. 7).

- [12] J. C. Sankey et al. “Strong and tunable nonlinear optomechanical coupling in a low-loss system”. In: *Nature Physics* 6.9 (June 2010), pp. 707–712 (cit. on pp. 9, 21).
- [13] J. D. Thompson et al. “Strong dispersive coupling of a high-finesse cavity to a micromechanical membrane.” In: *Nature* 452.7183 (Mar. 2008), pp. 72–75 (cit. on p. 21).
- [14] D. J. Wilson et al. “Measurement-based control of a mechanical oscillator at its thermal decoherence rate”. In: *Nature* (2015), pp. 2–6 (cit. on p. 21).
- [15] C. A. Regal, J. D. Teufel, and K. W. Lehnert. “Measuring nanomechanical motion with a microwave cavity interferometer”. In: *Nature Physics* 4.7 (May 2008), pp. 555–560 (cit. on p. 26).
- [16] R. A. Norte, J. P. Moura, and S. Gröblacher. “Mechanical Resonators for Quantum Optomechanics Experiments at Room Temperature”. In: *Phys. Rev. Lett.* 116 (14 Apr. 2016), p. 147202 (cit. on pp. 29, 30).
- [17] Guanhao Huang et al. “Room-temperature quantum optomechanics using an ultralow noise cavity”. en. In: *Nature* 626.7999 (Feb. 2024), pp. 512–516 (cit. on p. 29).
- [18] David Mason et al. “Continuous force and displacement measurement below the standard quantum limit”. en. In: *Nat. Phys.* 15.8 (Aug. 2019), pp. 745–749 (cit. on p. 29).
- [19] M. Underwood et al. “Measurement of the motional sidebands of a nanogram-scale oscillator in the quantum regime”. In: *Phys. Rev. A* 92 (6 Dec. 2015), p. 061801 (cit. on p. 29).

Sujet : Squeezed light optomechanics: Theory and Experiments

Résumé : Cette thèse de doctorat étudie les limites quantiques à l'oeuvre dans la détection interferométrique de petits déplacements mécaniques, et comment surmonter ces dernières en utilisant de la lumière comprimée. Dans un premier temps, le travail traite théoriquement la faisabilité d'une lumière comprimée dépendante en fréquence via l'utilisation d'une cavité de filtrage/rotation en sortie d'un amplificateur paramétrique optique. Dans un second temps, il se concentre sur la faisabilité d'une détection sous la limite quantique standard (SQL) en détaillant deux expériences réalisées. La première implémente un système « membrane at the edge » (MATE) basé sur une membrane en nitrure de silicium à haut facteur de qualité mécanique monté dans une cavité Fabry Perot de grande finesse. La deuxième expérience présente une source de lumière comprimée indépendante de la fréquence. Ces deux expériences sont pilotées à l'aide de locks optiques digitaux basé sur FPGA et développé au laboratoire, permettant un fonctionnement stable dans les conditions requises pour des mesures à la limite quantique.

Mots clés : Optomecanique, Lumière comprimée, Cavité de grande Finesse, Interferométrie, Bruit thermique, Bruit de grenaille quantique, Resonateur de grand facteur de Qualité, Interféromètres pour la detection d'ondes gravitationnelles, Bruit de pression de radiation quantique

Subject : Optomechanics and squeezed light

Abstract:

Keywords : Optomechanics, Squeezing, High-Finesse cavity, Interferometry, Thermal Noise, Quantum Shot Noise, High-Q Resonator, Gravitational wave Interferometer, Quantum Radiation Pressure Noise

